Research Square

Preprints are preliminary reports that have not undergone peer review.
They should not be considered conclusive, used to inform clinical practice,
or referenced by the media as validated information.

Hypothalamic c-FOS labeling after oral allulose and sucrose exposure in mice

Nancy Segura
Universidad Católica de la Santísima Concepción
Antonia Recabal-Beyer
Universidad de Concepción
Francisca Espinoza
Universidad Católica de la Santísima Concepción
Claudia Aguilera
Universidad Católica de la Santísima Concepción
Constanza Sanhueza
Universidad Católica de la Santísima Concepción
Bastián Aravena Sanzana
Universidad Católica de la Santísima Concepción
Rocío Belén Casas
Universidad Católica de la Santísima Concepción
Rocío Magdalena
Universidad Católica de la Santísima Concepción
Vinka Azócar
Universidad Católica de la Santísima Concepción
Isidora Troncoso
Universidad Católica de la Santísima Concepción
Aracelly Quiroz
Universidad de Concepción
Daniela Mennickent Barros
Universidad Católica de la Santísima Concepción
Ricardo Flores
Universidad San Sebastián
Roberto Elizondo
Universidad de Concepción
Danitza Vargas
Universidad de Concepción
María de los Ángeles García
Universidad de Concepción
Mauricio D Dorfman

UW Medicine Diabetes Institute, University of Washington

Joshua P Thaler

UW Medicine Diabetes Institute, University of Washington

Valentina González-Pecchi

Universidad Católica de la Santísima Concepción

Carlos Farkas

cfarkas@ucsc.cl

Universidad Católica de la Santísima Concepción

Article

Keywords: D-allulose, hypothalamus, c-FOS, feeding behavior, microglia, neuropeptide Y

Posted Date: November 6th, 2026

DOI: https://doi.org/10.21203/rs.3.rs-11219881/v1

License: This work is licensed under a Creative Commons Attribution 4.0 International License.
Read Full License

Additional Declarations: No competing interests reported.

Hypothalamic c-FOS labeling after oral allulose and sucrose exposure in mice

Nancy Segura[1], Antonia Recabal-Beyer[2], Francisca Espinoza[1], Claudia Aguilera[1], Constanza Sanhueza[1], Bastián Aravena Sanzana[1], Rocío Belén Casas[1], Rocío Magdalena[1], Vinka Azócar[1], Isidora Troncoso[1], Aracelly Quiroz[3], Daniela Mennickent Barros[1], Ricardo Flores[5], Roberto Elizondo[2], Danitza Vargas[2], María de los Ángeles García[2], Mauricio D Dorfman[4], Joshua P Thaler[4], Valentina González-Pecchi[1], Carlos Farkas[1*]

[1] Laboratorio de Investigación en Ciencias Biomédicas, Departamento de Ciencias Básicas y Morfología, Facultad de Medicina, Universidad Católica de la Santísima Concepción, Concepción, Chile

[2] Departamento de Biología Celular, Facultad de Ciencias Biológicas, Universidad de Concepción, Concepción, Chile

[3] Departamento de Especialidades, Facultad de Medicina, Universidad de Concepción, Concepción, Chile

[4] UW Medicine Diabetes Institute, Division of Metabolism, Endocrinology and Nutrition, Department of Medicine, University of Washington, Seattle, WA, USA

[5] Faculty of Economics and Business, Universidad San Sebastián, Concepción, Chile

*Correspondence: Carlos Farkas; cfarkas@ucsc.cl

ORCID: Antonia Recabal-Beyer: 0000-0003-2883-4739; Francisca Espinoza: 0000-0001-7059-6741; Claudia Aguilera: 0009-0001-5026-5678; Constanza Sanhueza: 0009-0007-9002-0505; Bastián Aravena Sanzana: 0009-0000-2324-1825; Rocío Belén Casas: 0009-0000-2983-4824; Rocío Magdalena: 0009-0002-6172-5251; Vinka Azócar: 0009-0005-2439-9321; Aracelly Quiroz: 0009-0000-5221-4762; Daniela Mennickent Barros: 0000-0002-6962-7632; Ricardo Flores: 0000-0002-9466-3993; Roberto Elizondo: 0000-0001-9790-0002; María de los Ángeles García: 0000-0001-8482-0361; Mauricio D Dorfman: 0000-0002-9587-0564; Joshua P Thaler: 0000-0002-8691-7340; Valentina González-Pecchi: 0000-0002-9163-4118; Carlos Farkas: 0000-0002-6245-2622.

Research Article

Abstract

D-Allulose influences feeding and metabolism, but hypothalamic responses to oral exposure remain incompletely understood. We compared water, 10% sucrose and 13% D-allulose using

drinking assays, hypothalamic immunofluorescence and peripheral histology in mice. Sucrose showed the highest consumption and lowest accompanying chow intake, without significant differences in body-weight change. After fluid familiarization and oral challenge, allulose yielded the highest mean c-FOS co-labeling in neuropeptide Y (NPY)-positive cells, with an exploratory overall difference but nonsignificant pairwise comparisons. Spatial analysis suggested greater clustering of c-FOS-positive NPY cells under allulose (unadjusted $p = 0.0286$, Holm-adjusted $p = 0.0571$). Exploratory comparisons also showed higher arcuate c-FOS labeling with allulose than sucrose and higher proopiomelanocortin (POMC)-associated co-labeling than water, although regional omnibus tests were nonsignificant. POMC spatial organization and regional glial staining showed no significant differences. First exposure after a 16-hour fast produced no significant difference in ACTH/CLIP-associated c-FOS co-labeling. Computational histology showed greater relative representation of liver nuclei classified as epithelial-like under allulose. These findings characterize consumption patterns and suggest a spatially grouped NPY-associated response to oral allulose that warrants investigation with matched imaging and functional measurements.

Keywords: D-allulose, hypothalamus, c-FOS, feeding behavior, microglia, neuropeptide Y

1

Introduction

D-Allulose is a low-energy C-3 epimer of fructose used as a sugar substitute. Controlled human studies have reported reductions in postprandial glycemic responses when allulose was

consumed with sucrose or meals, although effects vary with dose, study population and outcome [1, 2, 3]. In mice, oral allulose promotes the release of glucagon-like peptide-1 (GLP-1) from intestinal enteroendocrine L cells and reduces short-term food intake through mechanisms involving vagal afferents [4, 5]. Intragastric allulose also increases GLP-1, cholecystokinin and peptide YY in humans [6]. These gastrointestinal responses provide a rationale for examining hypothalamic circuits that integrate metabolic signals to regulate feeding.

The arcuate nucleus of the hypothalamus (ARC) integrates circulating metabolic signals and neural inputs involved in feeding and peripheral metabolism [7]. Its heterogeneous agouti-related peptide/neuropeptide Y (AgRP/NPY) and proopiomelanocortin (POMC) populations participate in overlapping metabolic circuits [8, 9, 10]. AgRP/NPY neurons generally promote feeding whereas POMC-derived melanocortin signaling can suppress it. The activity of both populations also depends on sensory cues, nutritional state and time since ingestion. Food presentation rapidly changes AgRP and POMC calcium signals, while gastrointestinal nutrients sustain suppression of AgRP activity [11, 12, 13]. Experimental manipulation of these populations has further clarified their coordinated contributions to feeding and glucose regulation [14]. Accordingly, c-FOS co-labeling can help identify stimulus-responsive populations but does not directly establish hunger, satiety or reciprocal activity between AgRP/NPY and POMC neurons.

Direct neuronal exposure and oral administration address different routes of allulose action. Yada and colleagues demonstrated that allulose reduced calcium oscillations in a subset of isolated mouse ARC NPY neurons and increased intracellular calcium in a subset of POMC neurons [15, 16]. They also showed that intracerebroventricular allulose reduced food intake [15, 16]. Following oral administration, intestinal GLP-1 release and vagal afferent signaling provide a route through which gut exposure can influence feeding without requiring direct neuronal contact with allulose [4, 17, 18]. Moreover, radiotracer experiments using ^{14}C-labeled D-psicose (D-allulose) found lower brain-associated radioactivity than in blood, liver or kidneys after oral administration in rats [19]. No brain signal was detected after intravenous administration in mice followed by vascular

perfusion. Thus, peripheral signaling provides a plausible link between oral allulose and hypothalamic responses, while the contribution of direct neuronal exposure remains unresolved.

Glial cells also contribute to hypothalamic metabolic regulation. Radial-like cells tanycytes lining the third ventricle and median eminence (ME) participate in nutrient sensing and exchange at the brain–periphery interface [20, 21]. Also, astrocytes and microglia interact with neuronal populations involved in feeding [22, 23]. Importantly, experimental astrocyte stimulation can inhibit AgRP neurons, while meal-related hyperglycemia can alter glial coverage of POMC neurons [24, 25]. These interactions provide a rationale for examining glial staining and morphology alongside neuronal responses to oral sugar exposure.

Here, we combined drinking assays with hypothalamic and peripheral histology to compare responses to water, 10% sucrose and 13% D-allulose in mice. Single- and two-bottle assays characterized fluid consumption, solution selection, chow intake and body-weight change. Following fluid familiarization and an oral challenge, we quantified regional c-FOS labeling and its association with NPY-positive and POMC-positive cells. We examined both the frequency and spatial organization of co-labeling to determine whether differences in the proportion of labeled cells were accompanied by local clustering within these populations.

Also, we assessed accompanying glial features using Iba1 and GFAP immunofluorescence and computational analysis of microglial morphology. A separate cohort received its first sugar challenge after a 16-hour fast to examine c-FOS co-labeling in POMC-related cells identified by ACTH/CLIP immunoreactivity. Peripheral histology evaluated liver, kidney and spleen. Our analyses suggest greater spatial clustering of c-FOS-positive NPY cells under allulose and identify differences in consumption patterns and predicted hepatic nuclear composition across exposure conditions. The NPY-associated spatial pattern provides a basis for investigating whether oral allulose recruits spatially grouped hypothalamic neurons and how such responses might contribute to feeding regulation.

Results

Sucrose consumption was highest across the drinking assays and accompanied lower chow intake

We first compared fluid consumption and body-weight change during single-bottle exposure to water, 10% (w/v) sucrose or 13% (w/v) allulose. Measurements on days 1, 3 and 6 characterized the trajectories, with day 6 used for the primary comparisons. Cages were the independent units, and animal-level weight changes were averaged within each cage.

Cumulative fluid consumption over time is shown in **Figure 1A**. At day 6, sucrose had the highest mean consumption (107.0 mL/cage), compared with water (26.7 mL/cage) and allulose (38.8 mL/cage) **(Figure 1B)**. Consumption differed overall by one-way ANOVA ($p = 0.0102$) and exact cage-label permutation testing ($p = 0.00916$). Pairwise comparisons suggested higher sucrose consumption than either alternative, with Holm-adjusted $p = 0.0714$ for both contrasts. Complete cage measurements and statistical results are provided in **Supplementary Table S2**.

Body-weight trajectories are shown in **Figure 1C**. At day 6, mean body-weight change was −8.20% under allulose, −0.61% under water and +0.52% under sucrose, with substantial variation among allulose cages **(Figure 1D)**. The overall difference was not significant (ANOVA $p = 0.118$, exact permutation $p = 0.0742$).

Sex-stratified trajectories showed the greatest mean weight decrease in allulose-exposed males, as depicted in **Supplementary Figure S1C**. Sucrose-exposed females had the highest fluid consumption **(Supplementary Figure S2A)**. These patterns are descriptive because the female water group contained one cage and no treatment-by-sex interaction was tested. Animal and cage assignments are provided in **Supplementary Table S1**.

To examine solution selection when water remained available, we performed a seven-day two-bottle assay. Each cage housed two mice and received one water bottle plus a second bottle containing water, 10% sucrose or 13% allulose. Control cages therefore received two water bottles.

Bottle positions were alternated daily, and we measured consumption from each bottle, chow intake and body-weight change.

Mean consumption from the test bottle was 36.97 g/cage/day for sucrose, 10.01 for water and 11.70 for allulose **(Supplementary Figure S4A)**. Consumption from the accompanying water bottle is shown separately in **Supplementary Figure S4B**. Sucrose and allulose solutions accounted for 88.2% and 49.3% of total fluid intake, respectively. In control cages, consumption was nearly evenly divided between the two water bottles, with 51.6% consumed from the designated test bottle **(Supplementary Figure S4C)**.

Mean chow intake was approximately halved under sucrose (3.51 versus 7.10 and 7.14 g/cage/day under water and allulose, respectively) **(Supplementary Figure S4D)**. Overall differences were detected for solution consumption, solution fraction and chow intake (all ANOVA $p < 0.001$), although exact pairwise comparisons were nonsignificant. Body-weight change did not differ significantly ($p = 0.661$) **(Supplementary Figure S4E)**. These observations are consistent with partial substitution of liquid for solid dietary energy. Cage-level measurements and complete statistical results are provided in **Supplementary Table S2**.

Arcuate c-FOS labeling after oral challenge

We next examined whether oral allulose or sucrose exposure was associated with differences in hypothalamic c-FOS labeling. Mice received their assigned fluid—water, 10% sucrose or 13% allulose—for seven days, followed by two days with water. After a four-hour fast, each mouse received a 200-µL oral challenge with the same fluid used during familiarization **(Figure 2A)**.

We used nuclear c-FOS staining as a marker of stimulus-associated gene expression [26]. Automated segmentation followed by human review identified DAPI-labeled nuclei and c-FOS-positive nuclei within the ARC, ME, ventromedial nucleus (VMN) and adjacent tissue. The nuclear

maps show the reviewed anatomical boundaries used to assign nuclei to each region **(Figure 2B)**. Representative microscopy illustrates DAPI and c-FOS staining across the three exposure conditions **(Figure 2C)**. For each animal and region, we calculated the percentage of DAPI-labeled nuclei that were also c-FOS positive. The manual correction and model-retraining workflow is described separately in the Methods and illustrated in **Supplementary Figure S7A**.

In the ARC, this percentage averaged 8.05% under allulose and 3.83% under sucrose, a difference of 4.22 percentage points (unadjusted exact Mann–Whitney U $p = 0.0411$) **(Figure 2D)**. The overall comparison across water, sucrose and allulose was nonsignificant in the ARC (ANOVA $p = 0.133$) and the other regions examined. Thus, the pairwise comparison suggests a possible difference in arcuate c-FOS labeling between allulose and sucrose, although its unadjusted statistical support remains exploratory. Regional measurements, sample sizes and complete statistical results are provided in **Supplementary Table S3**.

NPY-associated labeling and spatial clustering after oral exposure

We next examined c-FOS co-labeling and spatial organization in NPY-GFP mice because AgRP/NPY neurons respond to both sensory and gastrointestinal food signals [11, 12, 13]. Representative microscopy shows NPY-GFP and c-FOS labeling **(Figure 3A)**. Reviewed nuclear-assignment maps illustrate the water condition **(Figure 3B)**, sucrose condition **(Figure 3C)** and allulose condition **(Figure 3D)**, respectively. Each animal contributed one accepted field, with endpoint-specific inclusion recorded in **Supplementary Tables S1 and S3**.

The mean c-FOS-positive fraction of NPY-positive cells was highest under allulose (25.4%), compared with water (12.5%) and sucrose (3.6%) **(Figure 3F)**. An exploratory overall difference was detected by an enumerated Welch permutation test ($p = 0.0167$), while pairwise comparisons were nonsignificant. The corresponding total c-FOS/DAPI fractions were 6.8%, 3.6% and 1.8% under allulose, water and sucrose, respectively (overall $p = 0.0747$) **(Figure 3E)**.

We next asked whether oral exposure was associated with differences in how c-FOS-positive cells were arranged within the sampled tissue, beyond differences in overall labeling frequency. For each animal, we counted pairs of c-FOS-positive cells located within a specified distance of one another, repeating this calculation over 20–150 μm. We compared these counts with those expected under random labeling, keeping the observed cell positions and total number of positive cells fixed. This approach assesses whether labeled cells occur close together more often than expected from their abundance and the underlying distribution of cells. An example within the NPY population illustrates the pair-counting procedure **(Figure 3G)**. The resulting clustering profiles were compared across exposure conditions using a global envelope test that evaluated the full distance range. For total c-FOS labeling, these profiles did not differ significantly among water, sucrose and allulose conditions (global envelope $p = 0.2201$) **(Figure 3H)**.

Within the NPY population, allulose showed a pattern of greater c-FOS-positive cell clustering, with exploratory statistical support (global envelope $p = 0.0286$, Holm-adjusted $p = 0.0571$) **(Figure 3I)**. The between-condition statistic exceeded the nominal envelope over 30–150 μm. This pattern suggests spatially grouped labeling within the NPY population and motivates functional investigation. Spatial comparisons included three animals per condition because two water fields contained fewer than two double-positive cells and could not yield clustering curves. Acquisition differences and uncertain cage independence are considered in the Discussion. Curves, pair counts, conditional moments and complete tests are provided in **Supplementary Table S3**.

POMC-associated c-FOS labeling and spatial organization

We next examined c-FOS co-labeling in POMC-immunoreactive cells after the same fluid-familiarization and oral-challenge protocol. We analyzed the ARC, where POMC neurons participate in feeding and metabolic regulation [9, 10, 14], and the adjacent ME, which contributes to communication between the brain and peripheral metabolic signals [20, 21]. Sections were obtained from wild-type and NPY-GFP mice. In both genotypes, POMC-immunoreactive cells

were identified using an anti-POMC antibody, and we quantified the proportion that also showed nuclear c-FOS staining.

A representative section from an allulose-exposed mouse illustrates how POMC-associated c-FOS labeling was identified. DAPI staining marks the nuclei (**Figure 4A**). The c-FOS channel shows nuclear immunoreactivity (**Figure 4B**), while the POMC channel identifies POMC-immunoreactive cells (**Figure 4C**). The segmentation map shows the objects retained for quantification and the anatomical boundaries used to assign them to the ARC or ME (**Figure 4D**). The merged image includes an enlarged example of a POMC-immunoreactive cell with nuclear c-FOS staining (**Figure 4E**). In this NPY-GFP mouse, the additional GFP channel identifies NPY-associated fluorescence used to apply the overlap-exclusion criterion described in the Methods (**Figure 4F**).

We first quantified total c-FOS labeling as the percentage of DAPI-labeled nuclei that were c-FOS positive. This measure showed no significant overall difference among exposure conditions in either the ARC or ME (**Figure 4G**). We then calculated the percentage of POMC-immunoreactive cells that also showed nuclear c-FOS staining. In the ARC, this percentage averaged 25.6% under allulose, 18.4% under water and 22.0% under sucrose (**Figure 4H**). The allulose–water difference was 7.2 percentage points, with an unadjusted exact Mann–Whitney U $p = 0.0476$. However, the overall comparison across the three conditions was nonsignificant ($p = 0.1765$), as was the allulose–water comparison using cage means ($p = 0.200$). The higher mean co-labeling under allulose therefore represents an exploratory observation.

We next examined whether exposure conditions differed in the spatial clustering of c-FOS-positive cells in the ARC, using the same distance-based approach over 20–150 μm. Total c-FOS clustering showed no significant difference among conditions (Holm-adjusted global envelope $p = 0.5855$) (**Figure 4I**). When the analysis was restricted to the POMC-immunoreactive population, clustering of c-FOS-positive cells also did not differ significantly (Holm-adjusted global envelope $p = 0.7354$) (**Figure 4J**). Sparse c-FOS/POMC co-labeling in the ME prevented the corresponding

spatial comparison. **Supplementary Table S3** provides the animal-level measurements, cell counts used as denominators, spatial results and sensitivity analyses examining cage-level aggregation and cell-size filtering.

First-exposure ACTH/CLIP-associated labeling showed no significant group differences

To complement the familiarized-challenge experiments, we examined responses to an initial oral challenge after a longer fast. An independent cohort received water, sucrose or allulose after 16 hours of fasting, without prior sugar familiarization. This fasting duration has been used to investigate allulose-associated feeding suppression [4], and POMC responses can vary with feeding state and the timing of measurement [11, 27]. In this cohort, we identified POMC-related cells using an ACTH/CLIP antibody that recognizes a sequence present in both the POMC precursor and its ACTH/CLIP products. The staining therefore detects POMC-related immunoreactivity without distinguishing the intact precursor from these processed peptides. Representative microscopy illustrates the ACTH/CLIP signal (**Supplementary Figure S5C**). The nuclear-classification map shows the labeling assignments and anatomical boundaries used for regional quantification (**Supplementary Figure S5D**).

We first calculated the percentage of DAPI-labeled nuclei that were c-FOS positive. This measure showed no significant overall difference among exposure conditions in either the ARC ($p = 0.641$) or ME ($p = 0.676$) (**Supplementary Figure S5G**). We then assessed c-FOS co-labeling within the ARC ACTH/CLIP-immunoreactive population. The percentage of these cells that also showed nuclear c-FOS staining did not differ significantly among conditions ($p = 0.550$) (**Supplementary Figure S5H**).

To examine how labeling was distributed across the tissue field, we divided each field into six radial shells containing approximately equal numbers of DAPI-labeled nuclei, after excluding the third ventricle. Within each shell, we calculated the percentage of DAPI-labeled nuclei that were c-FOS positive. These spatial profiles showed no significant group difference (BH-adjusted $q = 0.464$) (**Supplementary Figure S5I**). We also calculated the percentage of DAPI-labeled nuclei that were positive for both c-FOS and ACTH/CLIP within each shell. These double-positive profiles likewise showed no significant group difference (BH-adjusted $q = 0.464$) (**Supplementary Figure S5J**). Restricting the analyses to wild-type animals did not change the interpretation. **Supplementary Table S3** provides the regional counts, co-labeling fractions, radial-shell measurements and sensitivity analyses.

Regional glial intensity and predicted microglial morphology

We next examined Iba1 and GFAP staining and microglial morphology alongside the neuronal measurements because glial interactions can influence feeding-related ARC neurons [24, 25, 28]. Representative Iba1 staining shows microglial labeling within the reviewed anatomical regions **(Figure 5A)**. GFAP staining is illustrated separately **(Figure 5B)**.

The GFAP example illustrates background estimation and thresholding before regional intensity measurements **(Figure 5E)**. Separate channel maps show how the glial signals were assigned to anatomical regions **(Figure 5F)**. Background-corrected Iba1 intensity showed no significant overall differences in the ARC, ME or VMN **(Figure 5G)**. GFAP intensity also showed

no significant regional differences **(Figure 5I)**. All regional ANOVA p values for these two markers were ≥ 0.316.

We used TinyMorphCNN, a convolutional neural network trained for this study, to classify individual Iba1-positive cells into four predicted morphology categories: ramified, rod-like, "activated" and amoeboid. The workflow shows how individual cell images were extracted and classified **(Figure 5C)**. A representative section illustrates the proportion of cells assigned to each category **(Figure 5D)**. For treatment comparisons, we combined the percentages assigned to the "activated" and amoeboid categories. These labels describe predicted cell shapes and do not establish inflammatory or functional activation.

The combined percentage was numerically lowest under sucrose in both regions. In the ARC, it averaged 48.9% under sucrose, compared with 51.9% under water and 51.0% under allulose. In the ME, it averaged 43.3% under sucrose, compared with 50.7% under water and 49.9% under allulose **(Figure 5H)**.

Several pairwise comparisons between exposure conditions had unadjusted p values below 0.05 when animals were treated as the independent units. However, the overall comparisons across the three conditions were nonsignificant in each region, as were the analyses using cages as the independent units. Therefore, these morphology differences remain exploratory. **Supplementary Table S4** provides regional staining intensities, cell counts, morphology-class fractions and the complete animal- and cage-level statistical comparisons.

Morphometric classification showed greater agreement with human microglial labels

To assess how closely automated morphology classifications agreed with human assessment, we compared two approaches on the same set of human-reviewed microglial cells. The first assigned categories using quantitative cell-shape measurements and fixed classification rules. The second used image features extracted by the pretrained DINOv2 model as inputs to a classifier

[29]. This benchmark was separate from the TinyMorphCNN analysis used to compare morphology across exposure conditions.

The benchmark included 203 cells from 15 animals. We measured performance using balanced accuracy, which gives equal weight to the proportion of correctly classified cells in each morphology category. Balanced accuracy was 73.9% for the morphometric approach (95% animal-bootstrap interval 67.4–81.1%) and 57.0% for the DINOv2-based classifier (49.3–65.2%). The paired difference favored morphometry by 16.9 percentage points (95% interval 7.8–25.1), with uncertainty estimated by resampling animals **(Supplementary Figure S6A)**.

We then examined recall within each category, defined as the percentage of human-labeled cells that the automated method assigned to the same category. Morphometry had higher recall for ramified, rod-like and "activated" cells. The DINOv2-based classifier had higher recall for amoeboid cells, correctly identifying 74.6%, compared with 66.2% for morphometry **(Supplementary Figure S6B)**. These categories describe cell shape rather than functional activation.

The morphometric confusion matrix shows which human-assigned categories were correctly identified and which were confused with other categories **(Supplementary Figure S6C)**. The DINOv2 confusion matrix presents the corresponding pattern of correct assignments and classification errors **(Supplementary Figure S6D)**.

The DINOv2-based classifier was evaluated using nested leave-one-animal-out validation, with each animal's cells held out from classifier fitting when generating their predictions. The morphometric rules were not fitted to the human labels, although their unsupervised preprocessing used the complete cell collection. This difference in evaluation should be considered when interpreting the performance comparison. **Supplementary Table S4** provides the paired cell-level predictions, category-specific performance measures and bootstrap draws.

Allulose was associated with a shift in predicted hepatic nuclear composition

We next examined liver, kidney and spleen tissue from mice in the single-bottle experiment to assess whether fluid exposure was associated with differences in peripheral histology. Measurements were summarized for each animal, and treatment comparisons accounted for cohort. The sampling workflow illustrates how tissue regions and microscopic fields were selected for analysis (**Supplementary Figure S3A**). We assessed conventional hematoxylin and eosin (H&E) staining and morphology measures, together with the relative proportions of nuclear categories predicted by computational image analysis. To summarize differences in predicted nuclear composition, we calculated each animal's distance from the water-control reference for the corresponding organ. Larger distances indicate a composition that differs more from the water reference across the categories considered together (**Supplementary Figure S3B**). Representative H&E images show the tissue morphology and examples of liver nuclei assigned to the epithelial-like category (**Supplementary Figure S3C**). Principal-component plots provide a complementary visualization, with nearby points representing animals with more similar predicted nuclear compositions (**Supplementary Figure S3D**).

Conventional H&E measurements showed no significant treatment contrasts across the three organs after correction for multiple comparisons. For example, mean hepatic nuclear density was numerically lower under allulose than water, at 6,733 and 8,924 nuclei/mm², but this difference was nonsignificant after correction ($q = 0.23520$). Effect estimates and confidence intervals for the conventional histological measurements are shown **(Supplementary Figure S3E)**.

The composition analysis identified greater relative representation of nuclei classified as epithelial-like in the liver under allulose than water (cohort-adjusted ratio 4.06, 95% CI 2.22–7.42, global BH q = 0.02418) **(Supplementary Figure S3F)**. This ratio compares the epithelial-like category with the geometric mean of the nuclear categories included in the analysis. It therefore describes a difference in relative predicted composition and does not establish an increase in absolute hepatocyte number. No other predicted-composition contrast remained significant after global multiple-testing correction. **Supplementary Table S5** provides the animal-level histological measurements, predicted nuclear-category counts, composition values and cohort-adjusted statistical comparisons.

Discussion

This study characterizes behavioral, hypothalamic and peripheral responses to oral allulose and sucrose exposure. The central observation is a spatial pattern suggestive of greater clustering of c-FOS-positive NPY cells under allulose, accompanied by the highest mean c-FOS co-labeling within this population. Together, these observations raise the possibility that oral allulose is associated with spatially grouped responses within the NPY population. Distinct drinking patterns and a difference in predicted hepatic nuclear composition provide complementary findings, although their functional relationships with the hypothalamic observations remain to be established.

Sucrose showed the highest cumulative consumption in the single-bottle assay **(Figure 1B)**. Its preferential consumption was also apparent when water remained available in the two-bottle assay **(Supplementary Figure S4A)**. This was accompanied by approximately half the chow intake observed under water or allulose **(Supplementary Figure S4D)**, consistent with partial substitution of liquid for solid dietary energy. Similar reductions in chow intake have been reported during longer liquid-sucrose exposure, with the effects on total energy intake and adiposity depending on how sucrose is delivered [30]. The behavioral findings therefore emphasize the importance of

considering fluid and chow consumption together when interpreting responses to sweetened solutions.

Sustained solution selection also integrates more than immediate sweet-taste acceptance. Allulose activates the human T1R2/T1R3 receptor in a cellular assay [33], yet mice can show brief-access licking followed by conditioned avoidance after training with 8% allulose [34]. Adding allulose to sucrose likewise affects intake and preference differently across experimental settings [35]. Studies of sucralose further illustrate this dependence on exposure conditions. Although chronic exposure implicated NPF/NPY pathways [36], subsequent work attributed increased feeding in flies to reduced intake during the exposure period [37]. These findings highlight sweetener identity, post-ingestive consequences and exposure history as relevant context for the drinking patterns observed here.

Body-weight change did not differ significantly during the brief intervention. Longer studies have reported altered fat accumulation after four weeks of dietary allulose in rats [31] and weight reduction after ten days of allulose gavage in obese mice [32]. Differences in treatment duration, delivery and baseline metabolic state limit direct comparison with the present study. Our pilot-based simulations also indicated that detecting weight-change differences would require more independent cages **(Supplementary Figure S8B)** than detecting consumption differences **(Supplementary Figure S8A)**. These estimates can inform future behavioral studies, but they do not establish the adequacy of the neuronal sample sizes.

The NPY analysis adds a spatial dimension to the assessment of hypothalamic responses. Allulose produced the highest mean proportion of NPY-positive cells co-labeled with c-FOS, with an exploratory overall difference among exposure conditions **(Figure 3F)**. The distance-based analysis then asked whether positive cells were located near one another more often than expected given each animal's cell positions and number of labeled cells. It suggested greater NPY-associated clustering under allulose (unadjusted $p = 0.0286$, Holm-adjusted $p = 0.0571$) **(Figure 3I)**. By accounting for labeling abundance and the underlying distribution of cells, this analysis addresses

a feature that is not captured by co-labeling percentages alone. The resulting pattern provides a basis for testing whether spatially grouped NPY populations participate in responses to oral allulose. Demonstrating coordinated activity or anatomical connectivity would require additional measurements.

The interpretation of this pattern depends on the biological readout and sampling time. Higher ARC c-FOS labeling under allulose than sucrose provided an additional exploratory indication of differing arcuate responses. However, the 30–40-minute collection window and the measurement of c-FOS expression address a different aspect of neuronal responsiveness from calcium recordings during rapid responses to food cues and intestinal nutrients [11, 12, 13]. c-FOS reflects stimulus-associated gene expression and does not directly quantify firing rate or peptide release [26]. Consequently, greater NPY-associated labeling cannot by itself be interpreted as increased orexigenic output or a prediction of subsequent feeding.

Oral administration preserves exposure through the mouth and gastrointestinal tract and permits peripheral signals to contribute to hypothalamic responses. This distinguishes our approach from intracerebroventricular (ICV) administration, which delivers allulose directly into the central nervous system and has been shown to reduce food intake [15, 16]. Dose also matters when comparing oral challenges with direct neuronal experiments. Allulose reduced calcium oscillations in a subset of isolated NPY neurons at 56 mM [15], while POMC calcium responses were reported at 5.6–56 mM [16]. Our 26-mg oral challenge corresponds to 1.04 g/kg in a 25-g mouse, but this administered dose does not specify the concentration reaching hypothalamic cells. Oral studies implicate intestinal GLP-1 release and vagal signaling in feeding suppression [4, 5]. Intestinal distension [18], cooperation between GLP-1 and insulin at vagal afferents [17], and enteroendocrine–vagal transmission [38] offer candidate mechanisms through which peripheral exposure could influence hypothalamic responses.

Direct hypothalamic exposure remains an open question. Radiotracer studies detected low brain-associated radioactivity after oral dosing in rats and no detectable brain signal after

intravenous dosing followed by vascular perfusion in mice [19]. These measurements support investigating peripheral signaling, although whole-brain measurements cannot resolve exposure at the specialized ARC–ME interface [20, 21]. Evidence that intestinal uptake can involve GLUT5 [39] establishes a potential absorption mechanism, but local measurements of allulose would be needed to determine whether direct neuronal exposure contributes under the present conditions.

The four-hour fast was intended to standardize recent feeding while limiting the duration of imposed food deprivation. Combined with prior fluid familiarization and ingestion by licking from a pipette tip, this protocol captures features of episodic sweetener consumption relevant to human dietary exposure. Its translational relevance lies in the route and pattern of exposure. A four-hour fast in mice should not be assumed to reproduce the metabolic state of a human interval between meals.

The consistency of the NPY spatial pattern will also depend on controlling anatomical and technical variation. Spatial comparisons are sensitive to the tissue sampled and to differences among animals [40, 41]. Here, water acquisitions included different microscopes and staining batches, and cage membership was unavailable for the NPY analysis. Matching pixel size and using physically calibrated distances improved comparability, but could not eliminate differences in optical sectioning or labeling detection [42]. These considerations make matched acquisition, comparable anatomical sampling and independently assigned cages priorities for replication.

The POMC findings broaden the neuronal context without establishing a reciprocal response between the two populations. Mean POMC-associated co-labeling was higher under allulose than water, supported by an exploratory unadjusted contrast, while omnibus, cage-level and spatial comparisons were nonsignificant. Direct POMC calcium responses to allulose provide biological context [16], but POMC heterogeneity [9, 10] and coordinated AgRP/NPY–POMC contributions to feeding and glucose regulation [14] argue against interpreting their c-FOS patterns as a simple opposing switch. Measurements of activity and peptide output would help determine how the observed labeling relates to the functions of these populations.

No significant ACTH/CLIP-associated co-labeling difference was detected in the first-exposure cohort after a 16-hour fast **(Supplementary Figure S5H)**. Although this fasting duration matched a previous study of allulose-associated feeding suppression [4], post-challenge intake was not measured here. Exposure history, fixation and staining also differed from the familiarized cohorts, preventing attribution of their differing patterns specifically to familiarization. POMC-dependent feeding effects [27], allulose-associated FGF21/oxytocin responses [35] and human imaging responses [43] have been examined over different timescales. A matched time-course experiment would help determine whether the present sampling captured only part of the response.

The glial measurements provided no clear evidence of treatment-associated differences under the conditions examined. Regional Iba1 and GFAP intensities were nonsignificant, and nominal microglial morphology differences were unsupported by cage-level analyses. Although Iba1 participates in membrane remodeling and phagocytosis [44], staining intensity and predicted shape categories are insufficient to establish functional or inflammatory states [45, 46]. Astrocyte activity, glial coverage and microglial signaling can influence ARC circuits [24, 25, 28], while longer sucrose exposure can induce glial responses [47]. The current measurements therefore leave open the possibility of functional or later glial changes that were not resolved by this analysis.

The separate morphology benchmark showed greater agreement with the human reviewer for fixed morphometric classifications than for the tested DINOv2-based classifier. This suggests that explicit shape measurements can be useful for describing these images, while the performance comparison remains specific to the selected cells and evaluation procedures. Morphometric preprocessing included the complete cell collection, whereas DINOv2 classifier fitting excluded the animal being evaluated. The benchmark therefore does not establish general superiority of one approach, and it does not independently validate the TinyMorphCNN treatment analysis or any classifier as a measure of inflammation.

In organs collected from the single-bottle experiment, allulose was associated with greater relative representation of liver nuclei classified as epithelial-like **(Supplementary Figure S3F)**.

This finding concerns predicted nuclear composition and should be distinguished from an increase in hepatocyte number. Hepatic epithelial lineages include hepatocytes and cholangiocytes [48], but a classifier developed on human tumor tissue cannot establish these identities in normal mouse liver [49]. Hepatocyte binucleation further separates nuclear counts from cell counts [50]. The composition difference therefore identifies a feature for targeted validation with cell-specific markers and direct histological measurements.

This hepatic observation is relevant to previous reports of reduced lipid accumulation and altered PPARγ/CD36-related expression during longer allulose interventions in mice [51], glycogen and triglyceride changes in rats [52], and reversible changes in organ weight [53]. Hepatic immune and mitochondrial pathways have also been implicated during prolonged treatment [54]. These studies provide plausible directions for follow-up, although the present nuclear-composition measurement cannot distinguish changes in lipid storage, glycogen content, cell abundance or tissue injury. The absence of significant conventional H&E contrasts after correction further limits assignment of a specific hepatic mechanism.

Taken together, the findings support a testable hypothesis that oral allulose is associated with spatially organized responses within the hypothalamic NPY population. The study also documents distinct consumption patterns and a peripheral difference in predicted hepatic nuclear composition. Small samples, undocumented randomization and blinding, uncertain NPY cage independence and acquisition differences limit causal attribution. Replication with matched imaging and anatomical sampling, combined with neuronal activity measurements and post-challenge feeding assays, would establish whether the NPY spatial pattern is reproducible and relevant to feeding regulation.

Methods

Animals, ethics and study organization

We used male and female NPY-GFP mice (B6.FVB-Tg(Npy-hrGFP)1Lowl/J, stock 006417), POMC-GFP mice (C57BL/6J-Tg(Pomc-EGFP)1Low/J, stock 009593) and C57BL/6J wild-type mice. All mice were purchased from The Jackson Laboratory and transferred to the Centro Regional de Estudios Avanzados para la Vida animal facility at Universidad de Concepción, Chile (CREA-V UdeC). Single-bottle animals were one year old, first-exposure ACTH/CLIP animals were 14 weeks old, and other cohorts were 11–14 weeks old. We housed the animals at the Centro Regional de Estudios Avanzados para la Vida, Universidad de Concepción, at 25 °C on a 12-hour light/dark cycle, with standard chow and assigned fluids except during fasting. All experimental protocols were approved by the Scientific Ethics Committee of Universidad Católica de la Santísima Concepción, Chile, for the project "Role of allulose in hypothalamic neuronal activation" (ORD. No. 18/2025). All methods were performed in accordance with the relevant guidelines and regulations.

The study included behavioral experiments, hypothalamic measurements after a familiarized oral challenge, an independent first-exposure cohort and peripheral histology. Mounted neuronal sections came from the single-bottle protocol, while the two-bottle cohort supplied POMC and glial tissue. Endpoint inclusion depended on available image channels, anatomy and valid denominators. Supplementary Table S1 lists animal identifiers, genotype, sex, cage, treatment and inclusion. The primary single-bottle weight analysis included 24 animals in 12 cages. Six additional water animals were analyzed separately. The two-bottle assay included 16 animals in eight cages. POMC immunofluorescence included wild-type and NPY-GFP mice. Randomization and treatment blinding were not documented. Reporting follows the relevant ARRIVE 2.0 items [55].

We extracted genomic DNA from approximately 2 mm of tail tissue in 75 µL of 25 mM NaOH/0.2 mM EDTA at 95 °C for one hour. We cooled samples to 15 °C, neutralized them with

75 µL of 40 mM Tris-HCl (pH 5.5) and centrifuged them at 4,000 rpm for three minutes at room temperature. We stored supernatants at −20 °C. The NPY assay used 3 µL DNA with primers oIMR6223 (5′-TATGTGGACGGGGCAGAAGATCCAGG-3′), oIMR6224 (5′-CCCAGCTCACATATTTATCTAGAG-3′) and oIMR6225 (5′-GGTGCGGTTGCCGTACTGGA-3′). PCR began at 95 °C for two minutes, followed by 35 cycles of 95 °C for 15 seconds, 57 °C for 15 seconds and 72 °C for 30 seconds. The final extension was 72 °C for five minutes.

The POMC assay used forward 5′-CTGTCCTCAGAAAGCCTTGG-3′ and reverse 5′-CTGAACTTGTGGCCGTTTAC-3′ primers, with internal-control primers 5′-CAAATGTTGCTTGTCTGGTG-3′ and 5′-GTCAGTCGAGTGCACAGTTT-3′. We resolved products in 2% agarose in 1× TAE using MaestroSafe stain (031201), 6× Purple loading dye (B7025S) and a FlashGel 100-bp–4-kb marker (50473), at 100 V for 40 minutes in a Wide Mini-Sub Cell GT system (1704401), and imaged them with an Omega Lum G system. Supplementary Table S1 lists genotype assignments.

Solution exposure and behavioral measurements

We assigned mice to water, 10% (w/v) sucrose or 13% (w/v) D-allulose, prepared with 10 g sucrose or 13 g allulose per 100 mL final solution. IANSA, Chile, supplied both sugars. The manufacturer’s certificate of analysis provided by IANSA reported an allulose purity of 98.53% on a dry basis. The study did not establish that the solutions were matched in sweetness, energy or osmolarity. During familiarization, mice received their assigned fluid and standard chow for seven days, followed by two days with water. After a four-hour fast, we placed a cut pipette tip at each animal's mouth and allowed it to lick the complete 200-µL contents, supplying 20 mg sucrose or 26 mg allulose. The independent first-exposure ACTH/CLIP cohort followed a separate protocol.

We estimated fluid consumption per cage from the change in bottle volume in the single-bottle experiment and bottle mass in the two-bottle experiment, without independent correction for unmeasured fluid losses. For the single-bottle experiment, cumulative consumption was baseline volume minus remaining volume, without conversion from mass. Twelve cages contributed

(water/sucrose/allulose, 3/5/4), with 5/9/10 animals providing complete series of positive weight measurements. We calculated each animal's percentage weight change from baseline, averaging these changes within its cage and weighted cage means equally. We treated nonpositive weight entries as invalid.

One animal, FR5-4, was transferred from allulose cage E2 to water cage E10 for dehydration immediately after the day-6 measurement. Its pre-transfer measurements remained assigned to allulose, and later weights were excluded from the primary analysis. E10/FR6-2 was assigned to water. Supplementary Tables S1 and S2 record the transfer and endpoint exclusions.

The two-bottle assay included eight cages with two mice per cage. Control cages received two water bottles, and other cages received one water bottle and one assigned sugar-solution bottle. Bottle positions were alternated daily. We weighed bottles and food, excluded initialization entries and summarized seven daily observations per cage in g/cage/day. Weight change was calculated from the pre-exposure baseline. Solution fraction was the mass change in the assigned bottle divided by the total change across both bottles. In controls, it describes consumption from the designated water bottle. Measurements, refill checks and cage summaries are provided in Supplementary Table S2.

Tissue collection and immunofluorescence

Thirty minutes after the familiarized oral challenge, mice received intraperitoneal ketamine (150 mg/kg) and xylazine (15 mg/kg), as used for pre-perfusion anesthesia by Recabal et al. [56]. We assessed anesthetic depth for up to ten minutes and confirmed deep anesthesia by the absence of pedal-withdrawal and blink reflexes. Animals were then euthanized by terminal transcardial perfusion under deep anesthesia. After priming the line, we cannulated the left ventricle of the heart and opened the right atrium. A perfusion pump delivered 10 mL cold PBS (pH 7.2–7.4), followed by 50 mL cold 4% paraformaldehyde in PBS. Liver blanching indicated the initial vascular wash.

We used a tissue chopper to isolate an approximately 2-mm coronal hypothalamic block between the optic chiasm and circle of Willis. We postfixed the blocks for 16 hours at 4 °C, cryoprotected them in 30% sucrose/PBS for five days at 4 °C and embedded them in OCT. For mounted preparations, we cut 20-µm coronal sections on a Leica CM1100 and stored them at −20 °C. The sampled interval was approximately bregma −1.23 to −2.15 mm. We cut floating 30-µm sections on a Leica SM2010R and stored them at −20 °C in phosphate-buffered cryoprotectant containing 30% sucrose and 30% ethylene glycol.

We washed mounted sections three times for five minutes in Tris–phosphate buffer (120 mM NaCl, 3.5 mM KH_2PO_4, 8.4 mM Na_2HPO_4 and 10 mM Tris, pH 7.8), then blocked them for one hour at room temperature in 0.3% Triton X-100 and 10% normal goat serum. We applied 60 µL primary-antibody solution per section and incubated for 16 hours at 4 °C in a humid, dark chamber. Primary antibodies were rabbit anti-c-FOS (Cell Signaling Technology, 31254S, 1:100) and mouse anti-NeuN (Sigma-Aldrich, MAB377, 1:200 or 1:250). Secondary antibodies were donkey anti-rabbit Alexa Fluor 647 (Jackson ImmunoResearch, 711-605-152, 1:200) and either anti-mouse Alexa Fluor 488 (Cell Signaling Technology, 4408, 1:200) or donkey anti-mouse Alexa Fluor 594 (Jackson ImmunoResearch, 715-585-150, RRID AB_2340854, 1:200). The experiments used both NeuN dilutions and secondary fluorophores. Secondary incubation lasted two hours at room temperature in darkness. We counterstained sections with DAPI (1:1000) for five minutes, washed them three times for five minutes and mounted them in Fluoromount-G (Electron Microscopy Sciences, 17984-25).

We washed floating sections five times for five minutes in PBS with agitation, then blocked them for one hour at room temperature in 2.5% normal donkey serum/0.5% Triton X-100. We incubated sections overnight at 4 °C with goat anti-c-FOS (Synaptic Systems, 226308, 1:1000), guinea-pig anti-POMC (Phoenix Pharmaceuticals, G-029-30, 1:4000), rabbit anti-Iba1 (FUJIFILM Wako, 019-19741, 1:2000) or GFAP-Cy3 (Sigma-Aldrich, C9205, 1:2000). Secondary antibodies were anti-goat Alexa Fluor 555 (Invitrogen, A-21432, 1:500), donkey anti-guinea-pig Alexa Fluor

647 (Jackson ImmunoResearch, 706-605-148, 1:500) and donkey anti-rabbit Alexa Fluor 647 (Invitrogen, A-31573, 1:500). Secondary incubation lasted one hour at room temperature with agitation in darkness. We mounted sections in DAPI Fluoromount-G. We used POMC immunostaining because we could not detect the intended reporter signal, including after anti-GFP amplification. Supplementary Table S6 provides the antibody inventory.

Microscopy, segmentation and anatomical review

Sucrose and allulose NPY fields were acquired on a Zeiss LSM 780 with an LD LCI Plan-Apochromat 25×/0.8 objective. Water fields were acquired on Leica SP8 microscopes at 20×/0.75 or 40×, or on the same Zeiss system and 25×/0.8 objective as the sugar fields. The two Zeiss water acquisitions used maximum-intensity projections of nine planes spaced 2.955 µm apart. Their 0.332106-µm pixels were reduced by 2×2 block averaging to match the 0.664213-µm sugar-image pitch before segmentation. Where necessary, one terminal row and column were removed to obtain even dimensions. The 40× water acquisition used a maximum-intensity projection of 21 planes. POMC and glial images were acquired on a Keyence BZ-X800. Per-animal acquisition and segmentation settings are provided in Supplementary Table S6. We segmented nuclei and marker-associated objects using custom Cellpose models and human-reviewed masks [57, 58, 59]. DAPI defined nuclei and supported manual delineation of ARC, ME, VMN and ventricular boundaries. Quantification used original-intensity channels independently of display normalization.

We registered POMC hemifields using DAPI and applied the same integer placement and seams to every channel and mask. The pipeline excluded c-FOS objects smaller than eight pixels and POMC instances overlapping NPY-GFP masks by at least 20%. The overlap rule defines image assignments and can remove genuine co-labeling, so it does not establish mutually exclusive cell identities. A second filter excluded POMC instances smaller than the mean DAPI nuclear area in the same section and anatomical region. We assigned objects to regions by their centroids and used their complete areas without clipping. The pipeline applied the size rule across conditions independently of c-FOS status and treatment statistics. Across 76 sections, it removed 780 of 3,403

processed POMC objects: 552 in ARC, 57 in ME and 171 outside delineated regions. Filtering left DAPI nuclei, original fluorescence and anatomical masks unchanged. POMC assignments and the outcomes that depended on them used the filtered labels. Supplementary Table S3 details object exclusions and sensitivity analyses across size thresholds.

Custom Cellpose models and review of segmentation masks

We refined Cellpose models through repeated segmentation, manual correction and fine-tuning. During review, masks were overlaid on the original fluorescence images to remove false objects, complete missing masks and merge fragments belonging to the same structure. Training used 42 nonduplicate TIFF image–mask pairs, excluding confocal acquisitions, and ran for 500–2,000 epochs depending on the model. Representative training images and reviewed masks are shown **(Supplementary Figure S7B)**. Training-loss curves illustrate model fitting across epochs **(Supplementary Figure S7C)**.

Models were selected according to the image channel and acquisition. NPY-GFP images were segmented using either a DAPI-trained or c-FOS-trained model, with a flow threshold of 0.4 and a cell-probability threshold of zero. Model identifiers, training images, epoch counts and acquisition-specific assignments are provided in **Supplementary Table S6**. Initialization, complete optimization settings and an independent evaluation set were not documented. Human review provided segmentation quality control.

In the NPY analysis, c-FOS regions smaller than five pixels were excluded, and assignment required at least 40% overlap with the best-matching DAPI nucleus. NPY assignment required at least one overlapping pixel and overlap equivalent to 5% of DAPI nuclear area. POMC size filtering was applied after segmentation without retraining. The analysis code uses Cellpose 4.2.1.1, while Keyence inference used Cellpose 4.0.7.dev18+g0a3de7b64.

Glial intensity and microglial morphology

We corrected Iba1 and GFAP signals for background in the native-intensity exports, divided the corrected signals by the area of each anatomical region and then aggregated measurements by animal. To construct GFAP masks, the pipeline subtracted background with a 35-µm gray opening and set the threshold to the larger of 0.8×Otsu or the median plus three normalized median absolute deviations. It removed objects smaller than 8 µm². All 61 included sections had reviewed anatomical masks, and unavailable regions remained missing. Supplementary Table S4 supplies regional intensities, predicted class fractions and sensitivity results.

TinyMorphCNN is a study-specific PyTorch convolutional network [60] with 79,780 trainable parameters. Its 96×96-pixel inputs contain Iba1 intensity, a cell mask and skeleton/distance features. Four 3×3 convolutional layers have 16, 32, 64 and 96 channels, with batch normalization and ReLU. The first three layers include 2×2 max pooling. Global average pooling, dropout of 0.25 and a linear layer produce probabilities for ramified, rod-like, "activated" and amoeboid morphology. Training used 17,112 morphometric pseudo-labeled cells from 15 animals with an 80/20 whole-animal split, class-weighted cross-entropy and AdamW [61]. Augmentation included flips, right-angle rotations and Iba1 intensity scaling of 0.85–1.15. The recorded run stopped at epoch 11 of a 25-epoch maximum, with minimum validation loss at epoch 5. Supplementary Table S6 gives the architecture and available training settings, distinguishing recorded values from implementation defaults. Treatment comparisons combined the predicted "activated" and amoeboid fractions. These categories describe cell shape, and the water cohort differed in sex and genotype composition.

Peripheral histology and the independent first-exposure cohort

We deparaffinized paraffin sections containing liver, kidney and spleen in successive Histo-Clear baths and rehydrated them through descending ethanol concentrations to water. After hematoxylin staining, we washed, differentiated and blued the sections, then stained them with eosin. We dehydrated sections through ascending ethanol concentrations, cleared them in Histo-

Clear and permanently mounted them. Twenty-four animal slides contained all three organs (water/sucrose/allulose, 7/9/8). We scanned whole slides with a 40× objective at 0.26178 µm/pixel using EasyScan 1.0.0 (build 1.0.0.58). We delineated each organ within its slide and sampled 24 spatially balanced, quality-controlled fields per organ at 0.5 µm/pixel. We summarized classical histological descriptors and HistoPLUS-predicted phenotypes by animal [49]. HistoPLUS development used human tumor tissue, so its class names describe predicted phenotypes in these mouse samples.

For each organ, we included phenotype classes that occurred in at least 18 of 24 animals and contained at least 24 objects in total. We calculated centered log-ratio composition using a 0.5 pseudocount only for these eligible classes. This expresses each predicted category relative to the geometric mean of the eligible categories, rather than as an absolute cell count. Ordinary least-squares (OLS) models included treatment and source cohort. We calculated HC3 confidence intervals and tested treatment contrasts with 99,999 Freedman–Lane residual permutations [62]. The reduced model retained source cohort and the other treatment contrast, and both observed and permuted statistics used HC3 standard errors. Permutation p values were (1 + number of equally or more extreme permutations)/(99,999 + 1), using seed 1707 and fixed endpoint-specific offsets.

We applied BH correction separately to three global families: 78 predicted-composition contrasts, including ineligible components assigned p=1, 36 classical H&E contrasts, and six water-reference deviation contrasts. The permutation procedure depends on the nuisance model and residual exchangeability. Supplementary Table S5 provides all measurements, principal-component and water-reference summaries, and statistical contrasts.

The independent first-exposure cohort included nine 14-week-old mice, three per condition, that fasted for 16 hours before receiving water, sucrose or allulose without prior sugar familiarization. Eight mice were wild type. The ninth, NPY-M, was a male NPY-GFP animal assigned to water. Mice received intraperitoneal ketamine (150 mg/kg) and xylazine (15 mg/kg). Deep anesthesia was confirmed by the absence of a pedal-withdrawal reflex in response to a foot

pinch before euthanasia by decapitation using long scissors. We fixed brains by immersion without vascular perfusion. Mouse monoclonal ACTH/CLIP F-3 (Santa Cruz Biotechnology, sc-373878, 1:100) recognizes an internal POMC epitope present in the precursor and its ACTH/CLIP products (https://datasheets.scbt.com/sc-373878.pdf). We used this antibody to identify POMC-related immunoreactivity in the first-exposure cohort. For NPY-M, the 488, 546 and 633 channels represented NPY-GFP, ACTH/CLIP and c-FOS, respectively. The analysis did not use NPY-GFP to classify either other marker.

Each animal contributed one acquisition. The size filter excluded ACTH/CLIP objects below the acquisition-specific fifth percentile of DAPI nuclear area (179/733 objects). Before spatial analysis, reviewed third-ventricle masks excluded 434 DAPI, zero c-FOS-positive and zero double-positive centroids. A sensitivity analysis included only the eight wild-type animals. ACTH/CLIP labeling served as an immunohistochemical endpoint, not a measurement of α-MSH release.

Internal comparison with human-reviewed microglial morphology

We compared morphometric and DINOv2 classifications with the same human-assigned morphology labels. A single observer completed reviews of 203 cells from 15 animals. These cells belonged to an initial selection of 300 cells, sampled with equal quotas for four proposed classes from a soma-refined collection of 14,415 Iba1-positive objects. The morphometric method standardized cell and branch measurements, grouped cells using four-cluster K-means and assigned morphology classes through a predefined cluster-to-class mapping. Human labels were not used to fit this method. However, its unsupervised preprocessing and clustering used the full collection, including animals represented in the reviewed sample. This benchmark was separate from the TinyMorphCNN treatment analysis.

For the image-based classifier, the pretrained DINOv2 ViT-S/14 encoder extracted features without updating its weights [29]. Each cell was represented by a target-cell crop and a wider-context crop, resized to 224 × 224 pixels and normalized using the encoder's channel means and

standard deviations. Class-token features and patch-token features weighted by the target-cell mask were averaged across four right-angle rotations and concatenated into 1,536 features per cell. Feature extraction used PyTorch 2.8.0+cu128 and an NVIDIA RTX A5000 GPU. **Supplementary Table S6** provides model and feature-extraction settings.

We evaluated the DINOv2 classifier using 15 leave-one-animal-out folds. In each fold, all reviewed cells from one animal were held out for evaluation. Only the remaining animals were used to fit feature standardization, whitened principal-component analysis with 32 components and class-balanced multinomial logistic regression. Three-fold stratified-group validation within the training animals selected the regularization parameter C from 0.1, 1 and 10. Logistic regression used L-BFGS, a maximum of 2,000 iterations, a tolerance of 10^{-6} and seed 20260907.

Performance was measured by balanced accuracy, the unweighted mean of the four class recalls. Recall is the proportion of cells in a human-assigned class that the method classified correctly. We estimated percentile 95% intervals for each method and their paired accuracy difference using 2,000 bootstrap samples of 15 animals drawn with replacement (seed 20260907). Every reviewed cell from each sampled animal was retained, and the same animal samples were used for both methods. Predictions remained fixed during resampling. The intervals therefore capture variation from animal sampling and do not include uncertainty from retraining. **Supplementary Table S4** provides confusion matrices, class recalls, paired predictions and bootstrap draws.

Statistical analysis and reproducibility

Cages were the independent units for shared behavioral measurements. Histological measurements were summarized by animal, with cells and sections treated as subsamples [63]. Where cage membership was known, additional cage-level analyses assessed whether the findings depended on treating animals as independent observations. Cage membership was unavailable for the NPY cohort, so possible dependence among animals sharing a cage remains a limitation. Sample sizes varied according to the available channels, accepted anatomical regions and valid

742 denominators. Each animal contributed one equally weighted curve to the NPY and POMC spatial
743 comparisons.

744 Unless otherwise specified, overall regional differences were assessed by one-way
745 ANOVA, and neuronal, glial and two-bottle pairwise comparisons used exact two-sided Mann–
746 Whitney U tests. Histological and two-bottle pairwise p values were unadjusted unless a correction
747 is stated and were interpreted as exploratory. The four regional c-FOS ANOVAs were corrected
748 together using Holm's method. Single-bottle outcomes used exhaustive cage-label permutation
749 tests, with the ANOVA F statistic for overall differences and the difference in means for two-sided
750 pairwise comparisons. Holm correction covered the three pairwise comparisons within each single-
751 bottle endpoint. Descriptive 95% intervals used 20,000 whole-cage bootstrap resamples, preserving
752 each cage's complete trajectory in longitudinal displays.

753 POMC cage-level sensitivity analyses compared cage means using exact two-sided Mann–
754 Whitney U tests. Glial sensitivity analyses used one-way ANOVA with equal weighting of cage
755 means. A separate glial analysis pooled morphology counts within cages and used exact cage-label
756 permutation tests of binomial deviance. Ratios with small positive denominators were retained, as
757 were finite values flagged by the Tukey 1.5-IQR rule. Ratios with zero denominators remained
758 undefined. We did not perform equivalence tests.

759 Sample-size scenarios used day-6 fluid consumption and cage-mean weight change from
760 the 12-cage single-bottle pilot: three water, five sucrose and four allulose cages. For each candidate
761 number of cages per group, we simulated 500,000 normally distributed datasets using the pilot
762 means, $\alpha = 0.05$ and a PCG64 generator (seed 20260908). With group-specific standard deviations
763 and Welch's ANOVA, power first reached 80% at five cages per group for consumption (80.16%)
764 and fourteen for weight change (80.77%). Assuming a common pooled residual variance and
765 ordinary ANOVA reduced these minimum group sizes to four cages for consumption and nine for
766 weight change.

An additional scenario assumed $\eta^2 = 0.21$, equivalent to Cohen's $f = \sqrt{[\eta^2/(1 - \eta^2)]} = 0.5156$. A noncentral F calculation gave 60.8% power with nine independent units per group and 82.8% with fourteen. These scenarios guide planning for overall behavioral treatment differences under the stated assumptions. They exclude allowances for attrition or multiple endpoints and neither estimate achieved power nor establish sample sizes for neuronal or glial outcomes. **Supplementary Table S6** provides the inputs and complete simulation results. The consumption power curves illustrate how power changes with the number of cages **(Supplementary Figure S8A)**. The corresponding curves address body-weight change **(Supplementary Figure S8B)**.

For the first-exposure ACTH/CLIP cohort, we assessed how labeling varied from the center toward the edge of each sampled field or section. Eligible DAPI nuclear centroids defined six concentric elliptical shells containing approximately equal numbers of nuclei. Elliptical partitioning has previously been used for equal-area compartments in studies of chromosome localization [64]. Here, shells were based on nuclear counts rather than equal areas. We centered the coordinates on their mean and transformed them using the eigenvectors and inverse square roots of the eigenvalues of their two-dimensional covariance matrix. This accounted for the orientation and elongation of the nuclear distribution. Quantiles of the transformed radial distances at 0, 1/6, 2/6, 3/6, 4/6, 5/6 and 1 defined the shell boundaries. Shells 1–2 contained approximately the inner third of eligible nuclei. Shell areas and thicknesses could vary, and marker positivity did not affect the boundaries.

Within each shell, we expressed c-FOS-positive or ACTH/CLIP/c-FOS double-positive nuclei as a percentage of its DAPI nuclei. Counts were first summed across corresponding shells within each animal, giving one six-value profile per animal for each endpoint. We compared conditions using Euclidean PERMANOVA [40] on arcsin-square-root-transformed proportions, enumerating 1,680 animal-label allocations. Benjamini–Hochberg (BH) correction covered the two spatial endpoints. Regional analyses for this cohort formed a separate BH family of 55 finite tests: 11 ANOVAs, 11 Kruskal–Wallis tests and 33 Mann–Whitney comparisons.

The familiarized NPY and ARC POMC cohorts used a distance-based analysis to ask whether positive cells occurred near one another more often than expected from the recorded cell positions and number of positive cells. Within each acquisition and tissue side, we counted positive–positive cell pairs separated by no more than r, using distances from 20 to 150 μm in 10-μm steps. For total c-FOS labeling, the reference positions were all DAPI-associated centroids. For marker-associated c-FOS labeling, they were the NPY-positive or POMC-positive centroids. The random-labeling model held these positions and the number of positive cells fixed while allowing positive labels to be reassigned among eligible positions.

We calculated the exact expected pair count and its variance under this model. Let T be the observed positive–positive pair count, P the number of all eligible pairs within r, Q the number of combinations of two eligible pairs sharing one cell, and $R = C(P, 2) - Q$ the number of combinations sharing no cells. Here, $C(P, 2)$ denotes the number of ways to choose two eligible pairs, and p_k is the probability that k specified cells are positive when m positive labels are assigned among N fixed positions. Then $E[T] = Pp_2$ and $E[T^2] = Pp_2 + 2(Qp_3 + Rp_4)$, with $\mathrm{Var}[T] = E[T^2] - E[T]^2$. Observed counts, expected counts and variances were summed across independent acquisition-and-side labeling strata before calculating each animal's standardized curve, $z(r) = (T - E[T])/\sqrt{\mathrm{Var}[T]}$. Positive z values indicate more nearby positive pairs than expected under random labeling. This calculation accounts for the recorded positions and positive-cell counts but cannot remove differences in detection, section depth or anatomical sampling. Only animals with finite values at every radius were included. Animals with fewer than two positive cells had no estimable curve and were not imputed.

We compared these spatial curves among conditions using a studentized maximum-deviation global envelope test [65]. At each radius, the one-way F statistic was standardized using its permutation mean and standard deviation. The largest standardized statistic across radii was then compared with its distribution across every animal-label allocation, including the observed allocation. The two NPY endpoints used 9,240 and 1,680 allocations, and the two POMC endpoints

used 168,168 and 60,060. Taking the maximum accounts for testing across radii. We then applied Holm correction across the two endpoints separately within each cohort. Invariant curves returned $p = 1$, while undefined statistics were treated as non-estimable.

Secondary NPY spatial measures used their stated four-test Holm families. Whole-field NPY fractions were compared using enumerated permutation tests with a Welch F statistic for overall differences and Welch t statistics for pairwise differences. **Supplementary Table S3** provides conventional tests, variance diagnostics, Hodges–Lehmann differences and Cliff's delta. Permutation inference assumes that observations are exchangeable under the null hypothesis. Studentization offers asymptotic robustness when distributions differ, but does not guarantee that protection in small samples [66].

Acknowledgements

We thank the staff of the Centro Regional de Estudios Avanzados para la Vida (CREA-V) for support with animal care, and the Centro de Microscopía Avanzada del Biobío (CMA Bío-Bío) for image acquisition, and colleagues who assisted with anatomical review and data organization.

Author contributions

N.S. and C.F. performed all experiments and carried out animal breeding, husbandry and data acquisition throughout the study. C.F. led experimental planning, data analysis, figure preparation and manuscript writing. A.R.-B. contributed to the conception of all experiments and performed all Apotome imaging. F.E. trained and assisted N.S. in microscope operation, immunohistochemistry and antibody staining. V.G.-P. assisted N.S. throughout the experimental work, except for the two-bottle experiment. M.D.D. conducted the two-bottle experiment. M.D.D. and J.P.T. assisted N.S. with brain sectioning, provided POMC, Iba1 and GFAP antibodies, supported Keyence imaging, and contributed to data analysis and interpretation.

R.E. proposed the 16-hour fasting experiment and GFAP/Iba1 imaging, provided reagents and laboratory space, and facilitated collaboration with M.D.D. M.A.G. provided the NPY transgenic mouse model and helped interpret the first experiment. D.V. assisted with breeding the NPY mouse colony and data analysis.

C.A., C.S., B.A.S. and R.B.C. assisted N.S. with immunohistochemical processing of peripheral tissues, H&E staining and slide-scanner imaging. A.Q. sectioned all peripheral organs, deparaffinized the sections, arranged access to the slide scanner, uploaded the images and contributed to data analysis.

R.M., V.A. and I.T. contributed to data analysis and manuscript writing. D.M.B. contributed to allulose purity analysis, statistical analysis and data interpretation. R.F. performed all deep-learning analyses and contributed to data interpretation. C.A., C.S., B.A.S., R.B.C., R.M., R.E., D.V., R.F., M.A.G., D.M.B. and V.G.-P. proofread the manuscript.

Data and code availability

Source data for **Figures 1–5** are deposited in Zenodo at https://doi.org/10.5281/zenodo.22265241. Source data for **Supplementary Figures S1–S5** are available at https://doi.org/10.5281/zenodo.22265243. Full-resolution H&E whole-slide image exports supporting **Supplementary Figure S3** are available at https://doi.org/10.5281/zenodo.22284125. The archived software and figure-reproduction package is available at https://doi.org/10.5281/zenodo.22265239.

Analysis code, current **Figures 3–4** cell coordinates and geometry, and microglial benchmark data are available at https://github.com/cfarkas/allulose-sucrose-hypothalamus/tree/a2057074b34cda18a5c83ad9cd5159375b76458f. Trained models are provided in the repository's models-2026-09-14 release. **Supplementary Tables S1–S6** contain the analysis datasets, statistical results and methodological settings. The two September 2026 water-control acquisitions are not included in the original Zenodo microscopy deposits.

Funding

This work was supported by ANID SIA/PAI 2021 (SA77210106), ANID FONDECYT Iniciación 2026 (11261618), and Universidad Católica de la Santísima Concepción through DI-REGULAR 2025.

References

1. Franchi, F. et al. Effects of D-allulose on glucose tolerance and insulin response to a standard oral sucrose load: results of a prospective, randomized, crossover study. BMJ Open Diabetes Res. Care 9, e001939 (2021). https://doi.org/10.1136/bmjdrc-2020-001939

2. Hayashi, N. et al. Study on the postprandial blood glucose suppression effect of D-psicose in borderline diabetes and the safety of long-term ingestion by normal human subjects. Biosci. Biotechnol. Biochem. 74, 510–519 (2010). https://doi.org/10.1271/bbb.90707

3. Fukunaga, K. et al. A pilot study on the efficacy of a diabetic diet containing the rare sugar D-allulose in patients with type 2 diabetes mellitus: a prospective, randomized, single-blind, crossover study. Nutrients 15, 2802 (2023). https://doi.org/10.3390/nu15122802

4. Iwasaki, Y. et al. GLP-1 release and vagal afferent activation mediate the beneficial metabolic and chronotherapeutic effects of D-allulose. Nat. Commun. 9, 113 (2018). https://doi.org/10.1038/s41467-017-02488-y

5. Masuda, Y. et al. Abilities of rare sugar members to release glucagon-like peptide-1 and suppress food intake in mice. Nutrients 17, 1221 (2025). https://doi.org/10.3390/nu17071221

6. Teysseire, F. et al. The role of D-allulose and erythritol on the activity of the gut sweet taste receptor and gastrointestinal satiation hormone release in humans: a randomized, controlled trial. J. Nutr. 152, 1228–1238 (2022). https://doi.org/10.1093/jn/nxac026

7. Jais, A. & Brüning, J. C. Arcuate nucleus-dependent regulation of metabolism-pathways to obesity and diabetes mellitus. Endocr. Rev. 43, 314–328 (2022). https://doi.org/10.1210/endrev/bnab025

8. Steuernagel, L. et al. HypoMap-a unified single-cell gene expression atlas of the murine hypothalamus. Nat. Metab. 4, 1402–1419 (2022). https://doi.org/10.1038/s42255-022-00657-y

9. Lavoie, O., Michael, N. J. & Caron, A. A critical update on the leptin-melanocortin system. J. Neurochem. 165, 467–486 (2023). https://doi.org/10.1111/jnc.15765

10. Sweeney, P., Gimenez, L. E., Hernandez, C. C. & Cone, R. D. Targeting the central melanocortin system for the treatment of metabolic disorders. Nat. Rev. Endocrinol. 19, 507–519 (2023). https://doi.org/10.1038/s41574-023-00855-y

11. Chen, Y., Lin, Y. C., Kuo, T. W. & Knight, Z. A. Sensory detection of food rapidly modulates arcuate feeding circuits. Cell 160, 829–841 (2015). https://doi.org/10.1016/j.cell.2015.01.033

12. Beutler, L. R. et al. Dynamics of gut-brain communication underlying hunger. Neuron 96, 461–475.e5 (2017). https://doi.org/10.1016/j.neuron.2017.09.043

13. Su, Z., Alhadeff, A. L. & Betley, J. N. Nutritive, post-ingestive signals are the primary regulators of AgRP neuron activity. Cell Rep. 21, 2724–2736 (2017). https://doi.org/10.1016/j.celrep.2017.11.036

14. De Solis, A. J. et al. Reciprocal activity of AgRP and POMC neurons governs coordinated control of feeding and metabolism. Nat. Metab. 6, 473–493 (2024). https://doi.org/10.1038/s42255-024-00987-z

915 15. Rakhat, Y. et al. d-Allulose inhibits ghrelin-responsive, glucose-sensitive and neuropeptide Y
916 neurons in the arcuate nucleus and central injection suppresses appetite-associated food intake in
917 mice. Nutrients 14, 3117 (2022). https://doi.org/10.3390/nu14153117
918 16. Yermek, R. et al. D-Allulose cooperates with glucagon-like peptide-1 and activates
919 proopiomelanocortin neurons in the arcuate nucleus and central injection inhibits feeding in mice.
920 Biochem. Biophys. Res. Commun. 613, 159–165 (2022).
921 https://doi.org/10.1016/j.bbrc.2022.04.027
922 17. Ohbayashi, K. et al. Gut-derived GLP-1 released by rare sugar d-allulose cooperates with insulin
923 to activate left-sided vagal afferents and enhance insulin sensitivity. Diabetes 75, 1086–1100
924 (2026). https://doi.org/10.2337/db25-1134
925 18. Mizuma, S., Hayakawa, M. & Hira, T. Intestinal distension induced by luminal D-allulose
926 promotes GLP-1 secretion in male rats. Endocrinology 166, bqaf002 (2025).
927 https://doi.org/10.1210/endocr/bqaf002
928 19. Tsukamoto, I. et al. Intestinal absorption, organ distribution, and urinary excretion of the rare
929 sugar D-psicose. Drug Des. Devel. Ther. 8, 1955–1964 (2014). https://doi.org/10.2147/dddt.s60247
930 20. Elizondo-Vega, R. et al. The role of tanycytes in hypothalamic glucosensing. J. Cell. Mol. Med.
931 19, 1471–1482 (2015). https://doi.org/10.1111/jcmm.12590
932 21. Clayton, R. W., Lovell-Badge, R. & Galichet, C. The properties and functions of glial cell types
933 of the hypothalamic median eminence. Front. Endocrinol. 13, 953995 (2022).
934 https://doi.org/10.3389/fendo.2022.953995
935 22. Nguyen, L. T. & Dodd, G. T. Hypothalamic neuronal-glial crosstalk in metabolic disease. npj
936 Metab. Health Dis. 2, 27 (2024). https://doi.org/10.1038/s44324-024-00026-1
937 23. Le Thuc, O., Lechner, F. M. & García-Cáceres, C. Hypothalamic astrocytes: connecting brain
938 and periphery in metabolic control. Rev. Endocr. Metab. Disord. 27, 421–434 (2026).
939 https://doi.org/10.1007/s11154-025-09995-0

24. Yang, L., Qi, Y. & Yang, Y. Astrocytes control food intake by inhibiting AGRP neuron activity via adenosine A1 receptors. Cell Rep. 11, 798–807 (2015). https://doi.org/10.1016/j.celrep.2015.04.002

25. Nuzzaci, D. et al. Postprandial hyperglycemia stimulates neuroglial plasticity in hypothalamic POMC neurons after a balanced meal. Cell Rep. 30, 3067–3078.e5 (2020). https://doi.org/10.1016/j.celrep.2020.02.029

26. Perrin-Terrin, A. S. et al. The c-FOS protein immunohistological detection: a useful tool as a marker of central pathways involved in specific physiological responses in vivo and ex vivo. J. Vis. Exp. (110), e53613 (2016). https://doi.org/10.3791/53613

27. Zhan, C. et al. Acute and long-term suppression of feeding behavior by POMC neurons in the brainstem and hypothalamus, respectively. J. Neurosci. 33, 3624–3632 (2013). https://doi.org/10.1523/jneurosci.2742-12.2013

28. Reis, W. L., Yi, C. X., Gao, Y., Tschöp, M. H. & Stern, J. E. Brain innate immunity regulates hypothalamic arcuate neuronal activity and feeding behavior. Endocrinology 156, 1303–1315 (2015). https://doi.org/10.1210/en.2014-1849

29. Oquab, M. et al. DINOv2: learning robust visual features without supervision. Trans. Mach. Learn. Res. (2024). https://openreview.net/forum?id=a68SUt6zFt

30. Togo, J., Hu, S., Li, M., Niu, C. & Speakman, J. R. Impact of dietary sucrose on adiposity and glucose homeostasis in C57BL/6J mice depends on mode of ingestion: liquid or solid. Mol. Metab. 27, 22–32 (2019). https://doi.org/10.1016/j.molmet.2019.05.010

31. Chen, J., Huang, W., Zhang, T., Lu, M. & Jiang, B. Anti-obesity potential of rare sugar d-psicose by regulating lipid metabolism in rats. Food Funct. 10, 2417–2425 (2019). https://doi.org/10.1039/c8fo01089g

32. Rakhat, Y. et al. D-Allulose reduces weight more persistently than oral semaglutide while both equally elevate grip strength in diet-induced obese mice. Nutrients 18, 707 (2026). https://doi.org/10.3390/nu18040707

966 33. Belloir, C., Jeannin, M., Karolkowski, A., Scott, C. & Briand, L. A receptor-based assay to
967 study the sweet and bitter tastes of sweeteners and binary sweet blends: the SWEET project. Chem.
968 Senses 49, bjae041 (2024). https://doi.org/10.1093/chemse/bjae041
969 34. Sclafani, A. et al. Conditioned preference and avoidance induced in mice by the rare sugars
970 isomaltulose and allulose. Physiol. Behav. 267, 114221 (2023).
971 https://doi.org/10.1016/j.physbeh.2023.114221
972 35. Efendi, O. G. H. N. B., Matsui, S., Tsuzuki, S. & Sasaki, T. Identification of FGF21-inducing
973 rare sugars that reduces sugar appetite in male BL/6 mice. Physiol. Rep. 13, e70618 (2025).
974 https://doi.org/10.14814/phy2.70618
975 36. Wang, Q. P. et al. Sucralose promotes food intake through NPY and a neuronal fasting response.
976 Cell Metab. 24, 75–90 (2016). https://doi.org/10.1016/j.cmet.2016.06.010
977 37. Park, J. H., Carvalho, G. B., Murphy, K. R., Ehrlich, M. R. & Ja, W. W. Sucralose suppresses
978 food intake. Cell Metab. 25, 484–485 (2017). https://doi.org/10.1016/j.cmet.2017.02.011
979 38. Kaelberer, M. M. et al. A gut-brain neural circuit for nutrient sensory transduction. Science 361,
980 eaat5236 (2018). https://doi.org/10.1126/science.aat5236
981 39. Kishida, K. et al. D-Allulose is a substrate of glucose transporter type 5 (GLUT5) in the small
982 intestine. Food Chem. 277, 604–608 (2019). https://doi.org/10.1016/j.foodchem.2018.11.003
983 40. Anderson, M. J. A new method for non-parametric multivariate analysis of variance. Austral
984 Ecol. 26, 32–46 (2001). https://doi.org/10.1111/j.1442-9993.2001.01070.pp.x
985 41. Anderson, M. J. Distance-based tests for homogeneity of multivariate dispersions. Biometrics
986 62, 245–253 (2006). https://doi.org/10.1111/j.1541-0420.2005.00440.x
987 42. Waters, J. C. Accuracy and precision in quantitative fluorescence microscopy. J. Cell Biol. 185,
988 1135–1148 (2009). https://doi.org/10.1083/jcb.200903097
989 43. Van Opstal, A. M. et al. Brain activity and connectivity changes in response to nutritive natural
990 sugars, non-nutritive natural sugar replacements and artificial sweeteners. Nutr. Neurosci. 24, 395–
991 405 (2021). https://doi.org/10.1080/1028415x.2019.1639306

992 44. Ohsawa, K., Imai, Y., Kanazawa, H., Sasaki, Y. & Kohsaka, S. Involvement of Iba1 in
993 membrane ruffling and phagocytosis of macrophages/microglia. J. Cell Sci. 113, 3073–3084
994 (2000). https://doi.org/10.1242/jcs.113.17.3073
995 45. Escartin, C. et al. Reactive astrocyte nomenclature, definitions, and future directions. Nat.
996 Neurosci. 24, 312–325 (2021). https://doi.org/10.1038/s41593-020-00783-4
997 46. Salvi, J. et al. Microgliosis: a double-edged sword in the control of food intake. FEBS J. 291,
998 615–631 (2024). https://doi.org/10.1111/febs.16583
999 47. Patkar, O. L. et al. A binge high sucrose diet provokes systemic and cerebral inflammation in
1000 rats without inducing obesity. Sci. Rep. 11, 11252 (2021). https://doi.org/10.1038/s41598-021-
1001 90817-z
1002 48. Aizarani, N. et al. A human liver cell atlas reveals heterogeneity and epithelial progenitors.
1003 Nature 572, 199–204 (2019). https://doi.org/10.1038/s41586-019-1373-2
1004 49. Adjadj, B. et al. Toward comprehensive cellular characterization of H&E slides. J. Pathol.
1005 Inform. 22, 100696 (2026). https://doi.org/10.1016/j.jpi.2026.100696
1006 50. Duncan, A. W. et al. The ploidy conveyor of mature hepatocytes as a source of genetic variation.
1007 Nature 467, 707–710 (2010). https://doi.org/10.1038/nature09414
1008 51. Yamazaki, M. et al. d-Allulose supplementation prevents diet-induced hepatic lipid
1009 accumulation via miR-130-mediated regulation in C57BL/6 mice. Mol. Nutr. Food Res. 67,
1010 e2200748 (2023). https://doi.org/10.1002/mnfr.202200748
1011 52. Cayabyab, K. B. et al. The metabolic and endocrine effects of a 12-week allulose-rich diet.
1012 Nutrients 16, 1821 (2024). https://doi.org/10.3390/nu16121821
1013 53. Ochiai, M. et al. Recovery of increased weights of the liver and kidneys by cessation of D-
1014 allulose feeding in Wistar rats. Fundam. Toxicol. Sci. 6, 217–224 (2019).
1015 https://doi.org/10.2131/fts.6.217
1016 54. Bae, H. R. et al. D-Allulose ameliorates dysregulated macrophage function and mitochondrial
1017 NADH homeostasis, mitigating obesity-induced insulin resistance. Nutrients 15, 4218 (2023).
1018 https://doi.org/10.3390/nu15194218

55. Percie du Sert, N. et al. The ARRIVE guidelines 2.0: updated guidelines for reporting animal research. PLoS Biol. 18, e3000410 (2020). https://doi.org/10.1371/journal.pbio.3000410

56. Recabal, A. et al. Connexin-43 gap junctions are responsible for the hypothalamic tanycyte-coupled network. Front. Cell. Neurosci. 12, 406 (2018). https://doi.org/10.3389/fncel.2018.00406

57. Stringer, C., Wang, T., Michaelos, M. & Pachitariu, M. Cellpose: a generalist algorithm for cellular segmentation. Nat. Methods 18, 100–106 (2021). https://doi.org/10.1038/s41592-020-01018-x

58. Pachitariu, M. & Stringer, C. Cellpose 2.0: how to train your own model. Nat. Methods 19, 1634–1641 (2022). https://doi.org/10.1038/s41592-022-01663-4

59. Pachitariu, M., Rariden, M. & Stringer, C. Cellpose-SAM: superhuman generalization for cellular segmentation. bioRxiv (2025). https://doi.org/10.1101/2025.04.28.651001 [Preprint]

60. Paszke, A. et al. PyTorch: an imperative style, high-performance deep learning library. Adv. Neural Inf. Process. Syst. 32 (2019). https://papers.neurips.cc/paper_files/paper/2019/hash/bdbca288fee7f92f2bfa9f7012727740-Abstract.html

61. Loshchilov, I. & Hutter, F. Decoupled weight decay regularization. International Conference on Learning Representations (2019). https://arxiv.org/abs/1711.05101

62. Winkler, A. M., Ridgway, G. R., Webster, M. A., Smith, S. M. & Nichols, T. E. Permutation inference for the general linear model. NeuroImage 92, 381–397 (2014). https://doi.org/10.1016/j.neuroimage.2014.01.060

63. Lazic, S. E. The problem of pseudoreplication in neuroscientific studies: is it affecting your analysis? BMC Neurosci. 11, 5 (2010). https://doi.org/10.1186/1471-2202-11-5

64. Mehta, I., Chakraborty, S. & Rao, B. J. IMACULAT - an open access package for the quantitative analysis of chromosome localization in the nucleus. PLoS One 8, e61386 (2013). https://doi.org/10.1371/journal.pone.0061386

65. Myllymäki, M., Mrkvička, T., Grabarnik, P., Seijo, H. & Hahn, U. Global envelope tests for spatial processes. J. R. Stat. Soc. B 79, 381–404 (2017). https://doi.org/10.1111/rssb.12172

66. Janssen, A. Studentized permutation tests for non-i.i.d. hypotheses and the generalized Behrens–Fisher problem. Stat. Probab. Lett. 36, 9–21 (1997). https://doi.org/10.1016/S0167-7152(97)00043-6

Figure

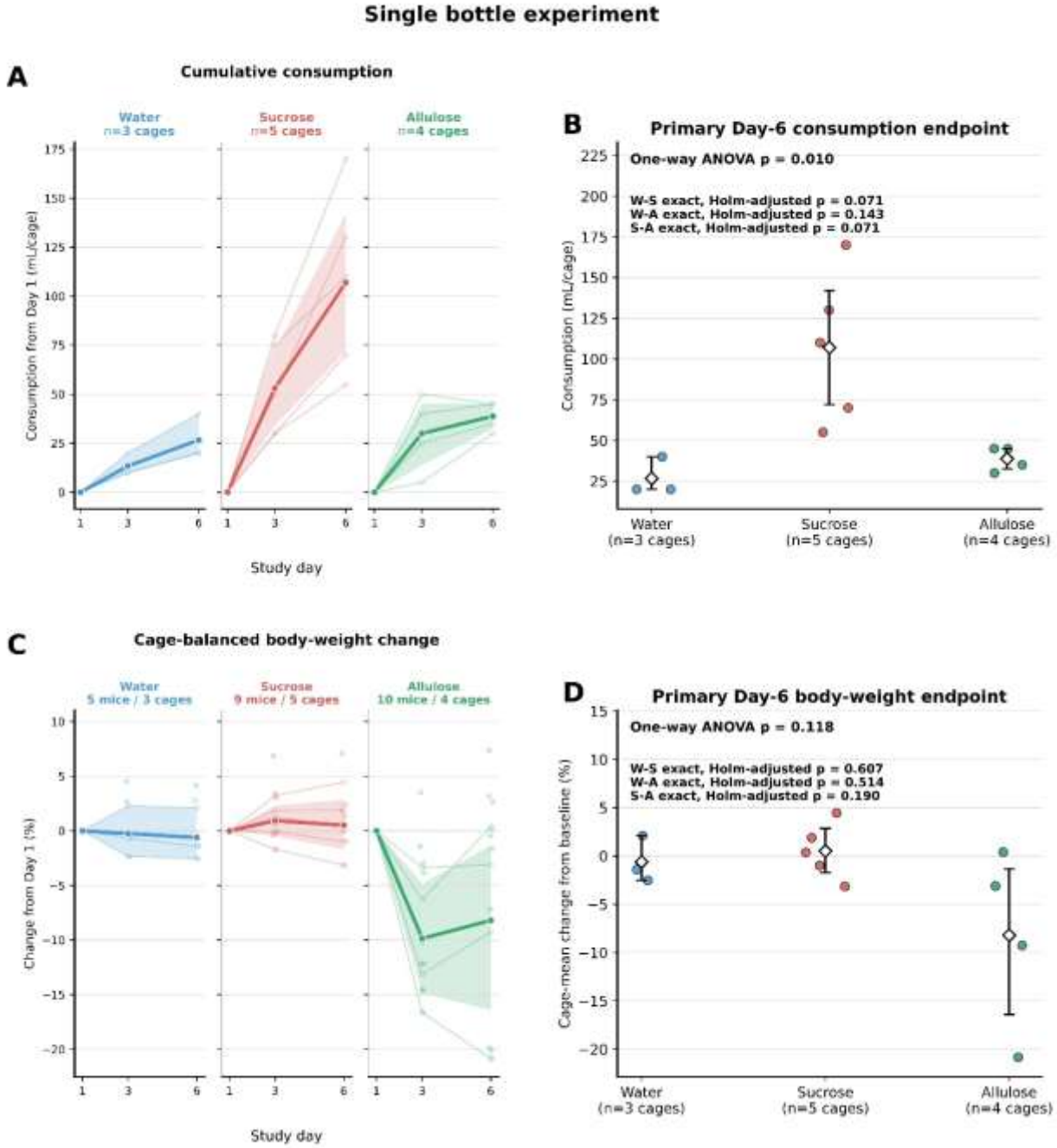


Figure 1 | Fluid consumption and body-weight change during single-bottle exposure.

Each cage received water, 10% (w/v) sucrose or 13% (w/v) allulose as its only drinking fluid. **A)** Cumulative fluid consumption from day 1, measured at days 1, 3 and 6. Thin lines trace individual cages, and thick lines show treatment means calculated with equal weighting of cages. **B)** Cumulative consumption at the primary day-6 endpoint, expressed as mL/cage. **C)** Percentage body-weight change from day-1 baseline. Faint points show individual animals, thin lines show cage means and thick lines show treatment means with equal weighting of cages. **D)** Day-6 cage-mean percentage weight change. Water, sucrose and allulose groups contributed 3, 5 and 4 cages, with weight measurements from 5, 9 and 10 animals. Points in B and D represent cages, and diamonds indicate group means. Shaded bands and whiskers show descriptive 95% intervals from 20,000 whole-cage bootstrap resamples. Overall comparisons used one-way ANOVA and exhaustive cage-label permutation of the F statistic. Pairwise comparisons used exact two-sided cage-label permutations of mean differences, with Holm correction across the three comparisons within each endpoint. Displayed overall p values are from ANOVA, and displayed pairwise p values are Holm-adjusted. W, S and A denote water, sucrose and allulose. Cage-level measurements, intervals and complete tests are provided in **Supplementary Table S2**.

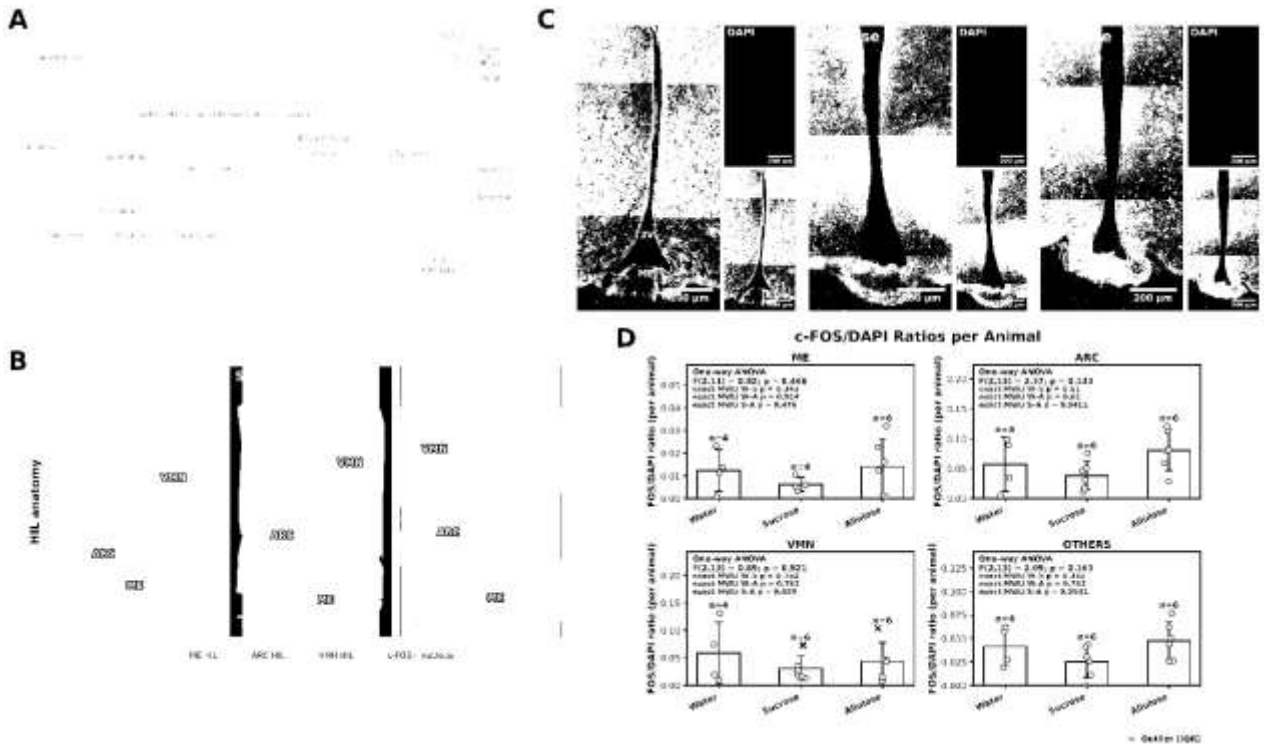


Figure 2 | Oral-challenge protocol and regional hypothalamic c-FOS labeling.

A) Familiarization and oral-challenge schedule. Mice received water, 10% (w/v) sucrose or 13% (w/v) allulose for seven days, followed by water for two days. After a four-hour fast, mice licked 200 µL of their familiarization fluid from a pipette tip. Anesthesia began 30 minutes later, followed by an anesthetic-depth assessment lasting up to 10 minutes and immediate perfusion. **B)** Nuclear-assignment maps showing c-FOS-positive nuclei and manually reviewed boundaries of the arcuate nucleus (ARC), median eminence (ME) and ventromedial nucleus (VMN). HIL denotes the human-in-the-loop review of anatomical boundaries. **C)** Representative fluorescence images for each condition, with merged DAPI/c-FOS images and separate channels. 3V denotes the third ventricle. **D)** Regional fraction of DAPI nuclei classified as c-FOS-positive. “OTHERS” denotes sampled tissue outside the delineated regions. Points represent animals, and bars show mean ± SD. Water, sucrose and allulose contributed 4, 6 and 6 animals in ARC, VMN and other tissue, and 4, 4 and 6 animals in ME. Crosses identify values flagged by the Tukey 1.5-IQR rule, which were retained. Displayed overall p values are from one-way ANOVA. Displayed W–S, W–A and S–A

comparisons use unadjusted exact two-sided Mann–Whitney U tests and are exploratory. **Supplementary Table S3** provides animal-level counts, denominators and complete comparisons, including Holm correction across the four regional ANOVAs. Scale bars: 200 µm.

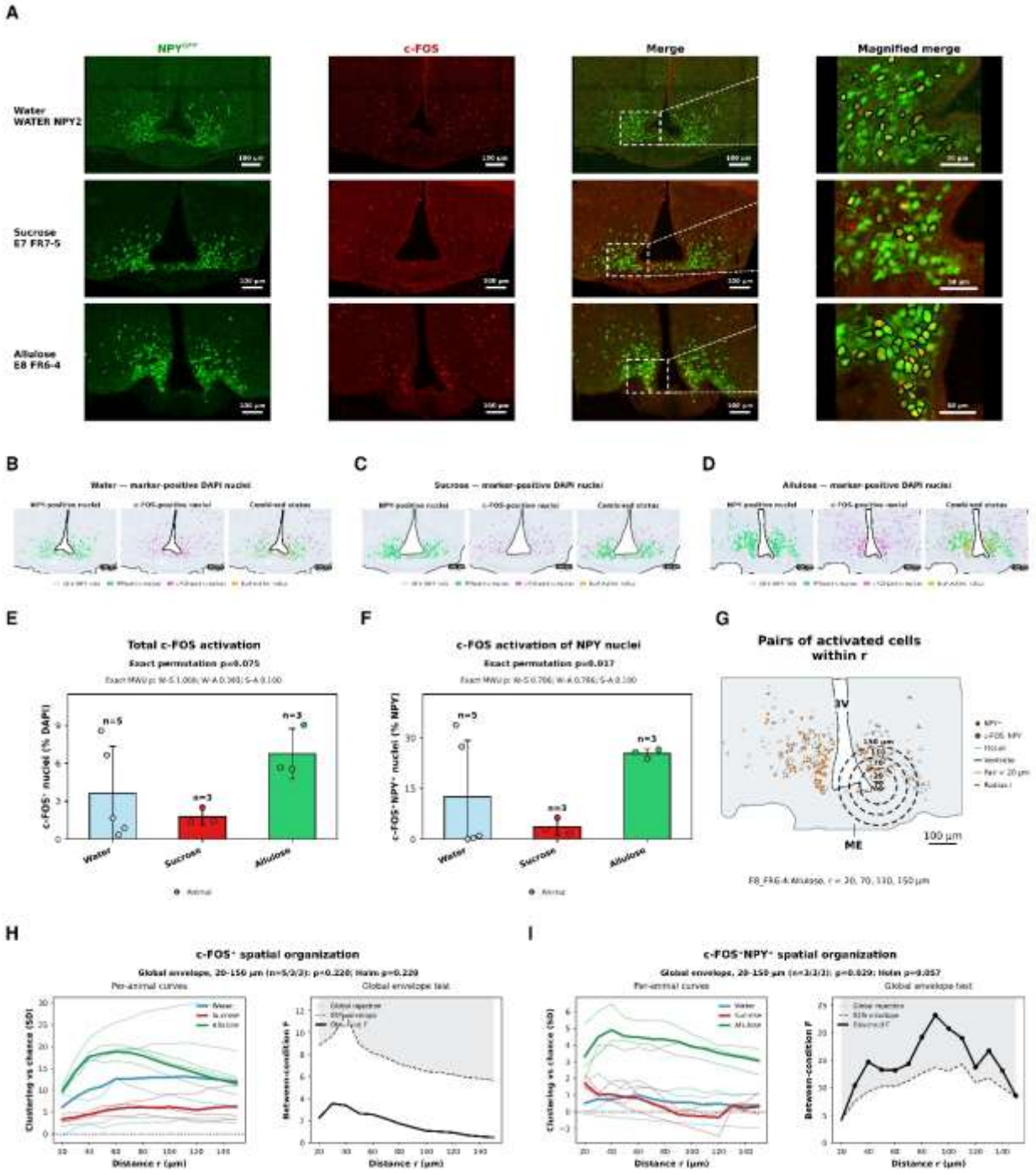


Figure 3 | NPY-associated c-FOS labeling and distance-dependent spatial clustering.

NPY-GFP mice were examined after fluid familiarization and oral challenge. **A)** Representative NPY-GFP and c-FOS fluorescence for each condition, with merged images and enlarged views. Black outlines in the enlarged views identify NPY-labeled regions assigned to c-FOS-positive nuclei. **B)** Nuclear assignments in a water field. **C)** Nuclear assignments in a sucrose field. **D)** Nuclear assignments in an allulose field. The maps distinguish c-FOS-positive nuclei, nuclei assigned to NPY-positive cells and double-labeled cells within reviewed tissue and ventricular boundaries. **E)** c-FOS-positive nuclei as a percentage of DAPI nuclei. **F)** Percentage of nuclei assigned to NPY-positive cells that were also c-FOS-positive. Points represent animals, and bars show mean ± SD. Both endpoints include 5 water, 3 sucrose and 3 allulose animals. Overall p values use exhaustive animal-label permutation tests of the Welch F statistic. The displayed pairwise p values use unadjusted exact two-sided Mann–Whitney U tests and are exploratory. **G)** Illustration of the pair-counting analysis in an allulose field. Orange points mark c-FOS-positive/NPY-positive centroids, and gray points mark NPY-positive centroids without c-FOS labeling. Orange segments connect positive pairs within 20 μm. Dashed circles illustrate the tested distances. **H)** Spatial clustering of c-FOS-positive nuclei among all DAPI-associated positions, including 5 water, 3 sucrose and 3 allulose animals. **I)** Spatial clustering of c-FOS-positive nuclei among NPY-positive positions, including 3 animals per condition. Two water animals had fewer than two double-positive nuclei and could not contribute to this endpoint. In H and I, thin curves show animals and thick curves show condition means. The vertical scale expresses excess positive-cell pairs in standard-deviation units relative to random labeling with each animal's observed positions and positive-cell counts held fixed. Values above zero indicate more nearby positive pairs than expected. Right-hand plots compare the observed between-condition F curve with its nominal global 95% envelope over 20–150 μm. Envelope tests account for the tested distances, followed by Holm correction across the two endpoints. Total c-FOS organization had Holm-adjusted $p = 0.2201$. The NPY-associated pattern suggested greater clustering under allulose (unadjusted $p = 0.0286$, Holm-adjusted p =

0.0571). Spatial proximity does not establish connectivity. **Supplementary Table S3** provides animal values, pair counts, spatial curves and complete tests. Scale bars: 100 µm for main fields and maps, 50 µm for enlarged views in A.

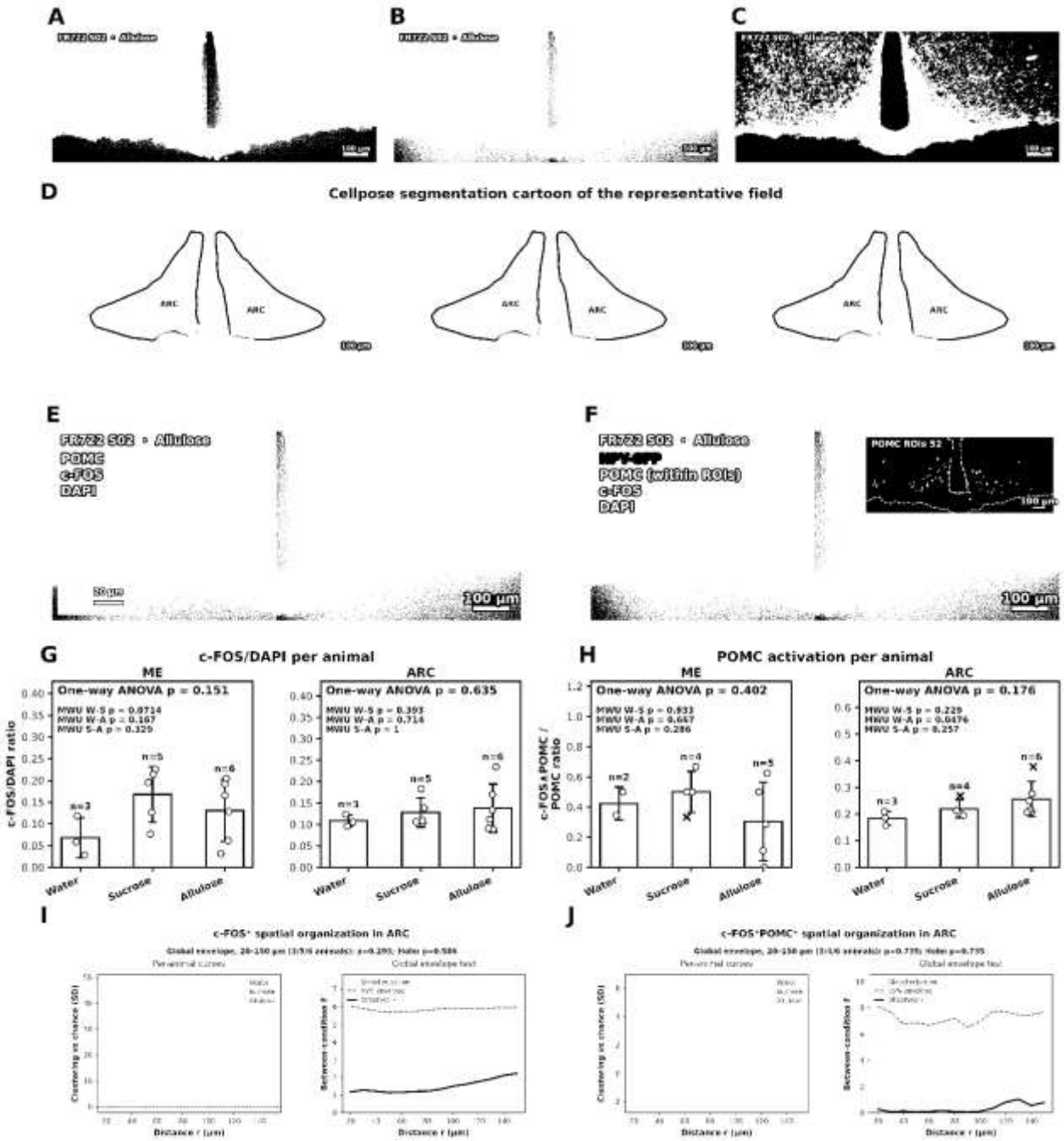


Figure 4 | POMC-associated c-FOS labeling and ARC spatial organization.

POMC-associated labeling was assessed in the ARC and adjacent ME after fluid familiarization and oral challenge. Representative images show an allulose-exposed NPY-GFP animal. **A)** DAPI

nuclear staining. **B)** c-FOS staining. **C)** POMC immunoreactivity. **D)** Accepted segmentation masks within reviewed ARC and ME boundaries. **E)** Merged channels, with an enlarged example of c-FOS/POMC co-labeling. **F)** Merged image including NPY-GFP, with an inset showing the marker regions used to assess NPY–POMC overlap. POMC display limits are matched between the main image and inset. Quantification used the NPY-overlap and DAPI-referenced POMC size filters described in Methods. **G)** Fraction of DAPI nuclei classified as c-FOS-positive, with 3 water, 5 sucrose and 6 allulose animals in each region. **H)** Fraction of POMC-positive cells co-labeled with c-FOS, with 3 water, 4 sucrose and 6 allulose animals in ARC, and 2 water, 4 sucrose and 5 allulose animals in ME. Points represent animals, bars show mean ± SD and crosses identify retained Tukey outliers. Overall p values use one-way ANOVA. Pairwise p values use unadjusted exact two-sided Mann–Whitney U tests and are exploratory. **I)** ARC clustering of c-FOS-positive nuclei among DAPI-associated positions, with 3 water, 5 sucrose and 6 allulose animals. **J)** ARC clustering of c-FOS-positive cells among POMC-positive positions, with 3 water, 4 sucrose and 6 allulose animals. Thin curves show animals, and thick curves show condition means. Curves express excess positive-cell pairs in standard-deviation units relative to random labeling with observed positions and positive-cell counts fixed. Values above zero indicate more nearby positive pairs than expected. Right-hand plots show the observed between-condition F curve and nominal global 95% envelope over 20–150 µm. Animal-label global envelope tests, followed by Holm correction across the two endpoints, gave adjusted $p = 0.5855$ in I and $p = 0.7354$ in J. Sparse marker-associated labeling precluded the corresponding ME spatial analysis. **Supplementary Table S3** provides animal-level measurements, denominators, spatial tests and cage- and size-filter sensitivity analyses. Scale bars: 100 µm for main fields, maps and the F inset, and 20 µm for the E inset.

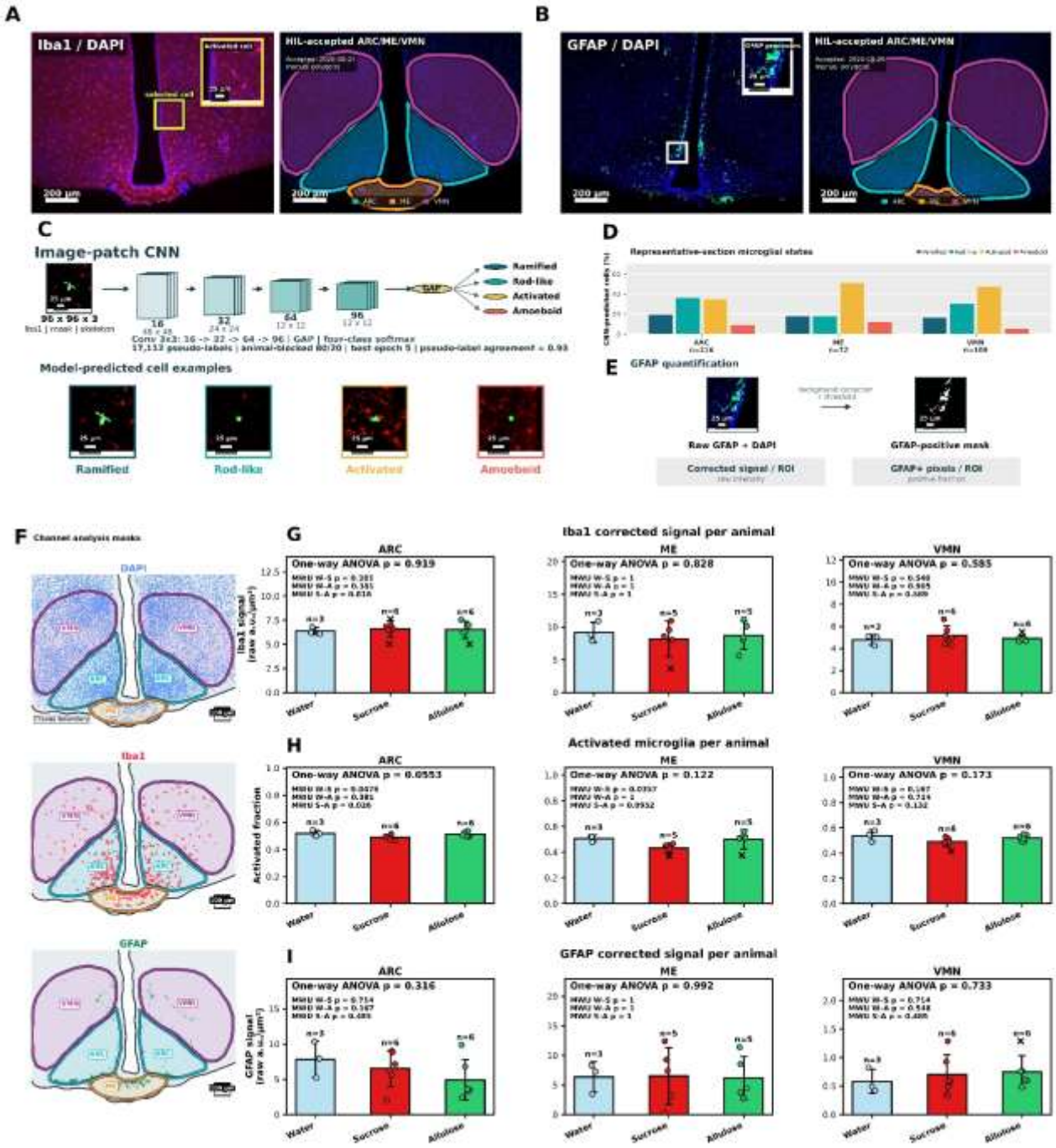


Figure 5 | Regional glial staining and predicted microglial morphology.

Iba1 and GFAP staining were assessed after fluid familiarization and oral challenge. **A)** Representative Iba1/DAPI fluorescence, an enlarged cell and reviewed anatomical boundaries. **B)** Corresponding GFAP/DAPI fluorescence, an enlarged view of labeled processes and reviewed boundaries. **C)** TinyMorphCNN workflow for classifying cropped Iba1-positive cells as ramified, rod-like, "activated" or amoeboid, with examples of predicted classes. GAP denotes global average

pooling. **D)** Predicted class percentages within each region of the representative section. **E)** GFAP background correction and identification of positive pixels. **F)** Separate DAPI, Iba1 and GFAP analysis masks. **G)** Background-corrected Iba1 signal divided by regional area. **H)** Fraction of all classified Iba1-positive cells assigned to either the "activated" or amoeboid shape class. The plotted "activated" fraction combines these two classes. **I)** Background-corrected GFAP signal divided by regional area. Morphology labels describe predicted shapes and do not establish inflammatory states. GFAP signal and positive area do not measure astrocyte number.

The analysis included 61 sections, summarized by animal. ARC and VMN included 3 water, 6 sucrose and 6 allulose animals. ME included 3 water, 5 sucrose and 5 allulose animals. Points represent animals, bars show mean ± SD and crosses identify retained Tukey outliers. Displayed tests are one-way ANOVA and exploratory, unadjusted exact two-sided Mann–Whitney U comparisons. **Supplementary Table S4** provides intensities, morphology counts and fractions, and animal- and cage-level tests. TinyMorphCNN development used 17,112 cells with morphometric pseudo-labels and an 80/20 training–validation split by animal. Its displayed pseudo-label agreement is distinct from agreement with human review, which was assessed for other classifiers **(Supplementary Figure S6)**. Scale bars: 200 μm in A and B, 100 μm in F and 25 μm in enlarged views and cell crops.

Supplementary Figures

Supplementary Figure S1 | Single-bottle consumption and body-weight change in males.

Male cages received water, 10% sucrose or 13% allulose as their only drinking fluid. **A)** Cumulative fluid consumption from day 1. **B)** Day-6 consumption in mL/cage. **C)** Percentage body-weight change from day-1 baseline. **D)** Day-6 cage-mean percentage weight change. The water group included 2 cages, sucrose 3 cages and allulose 2 cages. Weight measurements came from 2, 5 and 4 males in these groups. Thin lines show each cage's cumulative consumption in A and mean body-weight change in C. Thick lines show treatment means with equal weighting of cages. Faint points

in C show individual animals. Endpoint points represent cages, and diamonds indicate group means. Bands and whiskers show descriptive 95% intervals from 20,000 whole-cage bootstrap resamples. Displayed overall p values are from one-way ANOVA. Pairwise tests use exact two-sided cage-label permutations of mean differences with Holm correction across three comparisons per endpoint. **Supplementary Table S2** provides the observations, intervals and complete tests, including the exact omnibus permutation tests. These within-sex analyses are descriptive and do not test a treatment-by-sex interaction.

Supplementary Figure S2 | Single-bottle consumption and body-weight change in females.

Female cages received water, 10% sucrose or 13% allulose as their only drinking fluid. **A)** Cumulative fluid consumption from day 1. **B)** Day-6 consumption in mL/cage. **C)** Percentage body-weight change from day-1 baseline. **D)** Day-6 cage-mean percentage weight change. The water group included 1 cage, sucrose 2 cages and allulose 2 cages. Weight measurements came from 3, 4 and 6 females in these groups. Thin lines show each cage's cumulative consumption in A and mean body-weight change in C. Thick lines show treatment means with equal weighting of cages. Faint points in C show individual animals. Endpoint points represent cages, and diamonds indicate group means. Where estimable, bands and whiskers show descriptive 95% intervals from 20,000 whole-cage bootstrap resamples. The single water cage does not allow estimation of between-cage variability. Displayed overall p values are from one-way ANOVA. Pairwise tests use exact two-sided cage-label permutations of mean differences with Holm correction across three comparisons per endpoint. **Supplementary Table S2** provides the observations, intervals and complete tests, including the exact omnibus permutation tests. These within-sex patterns are descriptive and do not establish a treatment-by-sex interaction.

Supplementary Figure S3 | Liver, kidney and spleen histology after single-bottle exposure.

Liver, kidney and spleen were examined from animals in the single-bottle experiment: 7 water, 9 sucrose and 8 allulose animals. Each animal contributed all three organs, with 24 spatially balanced fields sampled per organ at 0.5 μm/pixel. **A)** Whole-slide workflow for locating organs, selecting

fields and obtaining animal-level measurements. **B)** Cross-validated Mahalanobis distance from the water-reference nuclear composition. Larger distances indicate greater multivariate deviation from that reference. Boxplots summarize the distributions, with individual animals overlaid as points. Displayed p values are from unadjusted one-way ANOVA. **C)** Representative H&E fields from the three organs and water/allulose liver examples highlighting nuclei classified as epithelial-like. Percentages in these example images describe the displayed fields. **D)** Principal-component plots of centered-log-ratio (CLR) nuclear composition, with one point per animal. **E)** Cohort-adjusted differences from water in conventional H&E measurements, expressed in units of each outcome's SD. **F)** Cohort-adjusted differences from water in CLR composition. Points or bars indicate effect estimates, and whiskers show heteroscedasticity-robust (HC3) 95% confidence intervals. Zero indicates no difference from water. Exponentiating a CLR effect gives the change in a category's representation relative to the geometric mean of eligible categories. The hepatic epithelial-like estimate for allulose corresponds to a ratio of 4.06 (95% CI 2.22–7.42, global Benjamini–Hochberg (BH) q = 0.02418), rather than a fourfold increase in cell number. Comparisons in E and F used 99,999 Freedman–Lane residual permutations, retaining cohort and the other treatment contrast in the reduced model. Stars in E denote unadjusted p values. Stars in F denote BH-adjusted q values across the 78 composition contrasts. One to four stars denote thresholds of 0.05, 0.01, 0.001 and 0.0001. No conventional H&E contrast retained significance after correction across its separate 36-test family. HistoPLUS categories are predicted nuclear phenotypes and do not establish cell identity. **Supplementary Table S5** provides measurements, phenotype counts, composition values and complete comparisons. Scale bars: 2 mm in A, 100 μm in the three-organ examples and 50 μm in the liver phenotype examples.

Supplementary Figure S4 | Fluid choice, chow intake and body-weight change in the two-bottle assay.

Each cage had simultaneous access to two bottles for seven days. One contained the assigned test fluid, water, 10% sucrose or 13% allulose, and the other contained water. Both bottles therefore

contained water in control cages. The water group included 2 cages, sucrose 3 cages and allulose 3 cages, with two animals per cage. **A)** Consumption from the designated test bottle. **B)** Consumption from the accompanying water bottle. **C)** Test-bottle consumption divided by total consumption from both bottles. A value of 0.5 indicates equal consumption from the two bottles. **D)** Chow consumption. **E)** Body-weight change from baseline, averaged within each cage. Fluid and chow intake are expressed as g/cage/day, while body-weight change is expressed in grams. Lines trace cages across study days. Summaries in A–D use one time-averaged value per cage over the seven-day observation period. The summary in E uses day-7 weight change averaged across the two animals in each cage. Day 0 provides baseline weight and is excluded from intake summaries. Summary points represent cages, with mean ± SD. W, A and S denote water, allulose and sucrose. Overall p values use one-way ANOVA, and pairwise p values use unadjusted exact two-sided Mann–Whitney U tests. Daily observations were not treated as independent replicates. **Supplementary Table S2** provides the daily records, cage summaries and statistical comparisons.

Supplementary Figure S5 | ACTH/CLIP-associated c-FOS labeling after first exposure and a 16-hour fast.

An independent cohort received water, sucrose or allulose after a 16-hour fast without prior sugar familiarization. Each group contained three 14-week-old animals. Eight animals were wild type, and one water-group animal was NPY-GFP. Each animal contributed one acquisition. ACTH/CLIP immunoreactivity identified POMC-related cells through an epitope present in the precursor and its ACTH/CLIP products. Representative images show an allulose-exposed animal. **A)** DAPI nuclear staining. **B)** c-FOS staining. **C)** ACTH/CLIP staining. **D)** Nuclear assignments and reviewed anatomical boundaries. **E)** Merged channels with enlarged co-labeling. **F)** ACTH/CLIP signal restricted to accepted cellular regions. **G)** Fraction of DAPI nuclei classified as c-FOS-positive in ME and ARC. **H)** Fraction of ACTH/CLIP-positive cells co-labeled with c-FOS in ARC. Points represent animals, and bars show mean ± SD. ANOVA and Kruskal–Wallis (KW) p values are unadjusted. The displayed sucrose–allulose Mann–Whitney U (MWU) q values use BH correction

across the 55 finite regional tests. Cliff's δ describes the corresponding pairwise effect size. **I)** Spatial distribution of c-FOS-positive nuclei. **J)** Spatial distribution of c-FOS/ACTH/CLIP double-positive nuclei. Upper maps provide descriptive views in normalized tissue coordinates, with the third ventricle excluded. Lower plots show labeling across six elliptical shells ordered from inner to outer and containing approximately equal numbers of eligible DAPI nuclei. Both spatial endpoints use the DAPI count in the same shell as denominator and are expressed as percentages. Thus, J describes double-positive nuclei relative to all eligible DAPI nuclei, whereas H describes co-labeling within ACTH/CLIP-positive cells. Thin lines show individual animals, thick lines show group means and heatmaps summarize the mean shell percentages. Shell boundaries were defined independently of marker positivity. ACTH/CLIP objects smaller than the acquisition-specific fifth percentile of DAPI nuclear area were excluded before analysis. Exact animal-label PERMANOVA of transformed six-shell profiles used 1,680 allocations, with BH correction across the two spatial endpoints ($q = 0.4643$ for each). **Supplementary Table S3** provides counts, profiles, complete tests and the wild-type-only sensitivity analysis. Scale bars: 100 µm in main images and 20 µm in enlarged views.

Supplementary Figure S6 | Agreement of microglial morphology classifiers with human review.

Fixed morphometric predictions and a logistic-regression classifier using frozen DINOv2 features were evaluated against the same labels from one human observer. The reviewed sample comprised 203 cells from 15 animals: 50 ramified, 32 rod-like, 50 "activated" and 71 amoeboid. These were the completed reviews from an initial selection of 300 cells with equal proposed-class quotas from 14,415 cells with refined soma boundaries. **A)** Balanced accuracy, calculated as the unweighted mean of the four class recalls, and the paired difference between methods. Whiskers show percentile 95% intervals from 2,000 paired whole-animal bootstrap samples. Predictions were held fixed, so these intervals reflect animal-sampling variation without retraining uncertainty. **B)** Recall within each human-assigned class, defined as the proportion classified correctly. **C)** Morphometric

confusion matrix. **D)** DINOv2 confusion matrix. Rows show human-assigned classes, and columns show predicted classes. Entries give cell counts and percentages within each row. Diagonal entries indicate agreement, and off-diagonal entries identify misclassifications. DINOv2 used nested leave-one-animal-out validation, with the evaluated animal excluded from all fitting and model selection. Morphometric labels were not fitted to human labels, although their unsupervised preprocessing used the full cell collection. This selected sample measures agreement with one reviewer's shape categories and does not estimate class prevalence or inflammatory state. The benchmark is separate from the TinyMorphCNN treatment analysis **(Figure 5)**. **Supplementary Table S4** provides paired predictions, class-specific results, confusion matrices and bootstrap draws.

Supplementary Figure S7 | Custom Cellpose training and manual review of segmentation masks.

A) Iterative workflow from initial segmentation to manual mask correction and model fine-tuning. Review removed false objects, added missing masks and merged fragments belonging to the same structure. **B)** Representative 512 × 512-pixel DAPI, c-FOS and POMC crops. The upper row shows fluorescence images, and the lower row overlays reviewed mask boundaries in green. Each image and its overlay use identical display limits at the 1st and 99.7th intensity percentiles. The POMC overlay also includes the subsequent size filter that removed objects smaller than the local mean DAPI nuclear area. This filtering did not retrain the models. **C)** Training-loss curves for five custom models, shown on a logarithmic vertical axis. One stored loss value corresponds to one epoch. The dapi_channel and cfos_channel3 runs contain 500 epochs, dapi_Keyence4 contains 1,000 epochs, and POMC_2 and cfos_Keyence1 contain 2,000 epochs. The curves describe model fitting and do not provide an independent estimate of segmentation accuracy. Training used 42 nonduplicate TIFF–mask pairs, excluding confocal acquisitions. **Supplementary Table S6** provides training-image inventories, model identifiers and available settings.

Supplementary Figure S8 | Pilot-based sample-size scenarios for behavioral outcomes.

Pilot measurements were used to estimate power for future balanced comparisons of water, sucrose and allulose. **A)** Day-6 cumulative fluid consumption. **B)** Day-6 cage-mean percentage body-weight change. The pilot contained 12 independent cages: 3 water, 5 sucrose and 4 allulose. Each candidate group size used 500,000 normally distributed simulations with the observed group means and $\alpha = 0.05$. Solid curves retain group-specific pilot standard deviations and use Welch's ANOVA. Dashed curves use a pooled common variance and ordinary ANOVA. The horizontal line marks 80% power, and points identify the smallest equal number of cages per group reaching that threshold. For consumption, the thresholds were 5 cages with group-specific variances and 4 with common variance. For weight change, they were 14 and 9 cages. These are planning scenarios under the pilot-based assumptions, without allowances for attrition or multiple endpoints. They do not estimate achieved power or establish sample sizes for neuronal or glial outcomes. **Supplementary Table S6** provides pilot values, simulation settings and complete results.

Supplementary Tables

Supplementary Table S1 | Animal and acquisition records across the study.

Animal and acquisition identifiers, treatment, genotype, sex, cage, cohort age and endpoint inclusion. Exclusion records and the documented cage transfer identify observations used in each analysis. Unknown metadata remain unassigned.

Supplementary Table S2 | Behavioral data, bottle-volume calculation and statistical results.

Original and processed fluid, food and body-weight measurements, cage-level summaries, exclusions, bootstrap intervals and statistical comparisons. The single-bottle data support **Figure 1**. Male-only analyses support **Supplementary Figure S1,** and female-only analyses support **Supplementary Figure S2**. The two-bottle measurements and analyses support **Supplementary Figure S4**. Units and analysis units are specified in each data table.

Supplementary Table S3 | Neuronal labeling and spatial-profile outcomes.

Regional cell counts and c-FOS labeling fractions support **Figure 2**. NPY-associated co-labeling and spatial analyses support **Figure 3**. POMC-associated co-labeling, spatial analyses and cage- and size-filter sensitivity analyses support **Figure 4**. Spatial datasets include animal-level curves, conditional pair moments, envelope tests and adjusted p values. First-exposure regional, shell-based and wild-type-only analyses support **Supplementary Figure S5**.

Supplementary Table S4 | Glial endpoints and microglial morphology classification.

Regional Iba1 and GFAP measurements, predicted morphology counts and fractions, animal- and cage-level tests and section inclusion for **Figure 5**. Paired human labels, classifier predictions, accuracy measures, confusion matrices and bootstrap draws support **Supplementary Figure S6**.

Supplementary Table S5 | Liver, kidney and spleen histology and predicted nuclear composition.

Animal and organ identifiers, conventional H&E measurements, predicted nuclear phenotype counts, centered log-ratio composition, principal-component scores and cohort-adjusted comparisons for **Supplementary Figure S3**. Water-reference distances and phenotype definitions are included.

Supplementary Table S6 | Experimental methods, antibody reagents and segmentation models.

Exposure and tissue-preparation protocols, antibody reagents, genotyping conditions, microscopy settings, segmentation models and training parameters. Pilot cage measurements, simulation settings and power curves support **Supplementary Figure S8**.

Supplementary Files

This is a list of supplementary files associated with this preprint. Click to download.

- SupplementaryTableS4Glialresults.xlsx
- SupplementaryTableS1Animalinventory.xlsx
- SupplementaryTableS6Methodsandmodels.xlsx
- SupplementaryTableS2Bottlerecords.xlsx
- SupplementaryTableS5Peripheralhistology.xlsx
- SupplementaryTableS3Neuronalresults.xlsx
- FigS1.tif
- FigS2.tif
- FigS6.tif
- FigS8.tif
- FigS4.tif
- FigS7.tif
- FigS5.tif
- FigS3.tif